

Competition for actin between two distinct F-actin networks defines a bistable switch for cell polarization

Alexis J. Lomakin^{1,2,6,7}, Kun-Chun Lee^{3,4,6,7}, Sangyoon J. Han^{1,7}, Duyen A. Bui¹, Michael Davidson⁵, Alex Mogilner^{3,4,7,8} and Gaudenz Danuser^{1,7,8}

Symmetry-breaking polarization enables functional plasticity of cells and tissues and is yet not well understood. Here we show that epithelial cells, hard-wired to maintain a static morphology and to preserve tissue organization, can spontaneously switch to a migratory polarized phenotype after relaxation of the actomyosin cytoskeleton. We find that myosin II engages actin in the formation of cortical actomyosin bundles and thus makes it unavailable for deployment in the process of dendritic growth normally driving cell motility. Under low-tractility regimes, epithelial cells polarize in a front-back manner owing to the emergence of actin retrograde flows powered by dendritic polymerization of actin. Coupled to cell movement, the flows transport myosin II from the front to the back of the cell, where the motor locally 'locks' actin in contractile bundles. This polarization mechanism could be employed by embryonic and cancer epithelial cells in microenvironments where high-tractility-driven cell motion is inefficient.

The inherent ability of some animal cell types to easily change shape and initiate polarized movements reflects their functional requirement to explore the space around them. On the other end of the spectrum are cell types, particularly differentiated ones such as epithelial cells, that maintain a static morphology to preserve tissue organization and function. However, during embryogenesis and carcinogenesis epithelial cells can spontaneously lose their organization and acquire anteroposterior polarity characteristic of mesenchymal cells¹. The cell shape changes are prerequisites for directional cell migration and adaptation to variable microenvironments. Characteristic molecular circuits regulating the epithelial cell morphodynamics involve members of the Rho family of small GTPases, which communicate polarity information to the actin cytoskeleton²⁻⁴. In tumour epithelial cells, RhoA GTPase stimulates actomyosin contractility, which rounds-up the cell, whereas Rac1 GTPase excites actin polymerization to enable the formation of polarized cell protrusions⁵. The two GTPases inhibit each other through intermediate biochemical reactions, and this reciprocal inhibitory crosstalk is predicted to effectively increase the signal gain in favour of either specific Rho-type or Rac-type cell morphologies⁶. A challenge in testing this model is that many of the molecular factors mediating

the inhibitory crosstalk have not been identified⁷. Moreover, the key events underlying large-scale cell reorganization after signal gain in favour of a specific GTPase are unknown. Therefore, in the present study, we set out to determine the fundamental organizing principles that link molecular activities of signalling systems to cell polarization.

RESULTS

Myosin II inhibits spontaneous symmetry breaking and motility initiation in epithelial cells

To understand how epithelial cells maintain and break their normal morphology, we performed experiments aimed at identifying a regulatory switch that excites cell shape polarization after turning on or off the activity of signalling circuits controlled by Rho GTPases. We analysed the degree of structural polarity in single non-tumorigenic rat liver epithelial cells, IAR-2, in different signalling states. Among the conserved Cdc42-, RhoA- and Rac1-mediated polarity pathways, the signalling cascade RhoA → Rho-kinase (ROCK) → myosin II regulatory light chain (MRLC) emerged as a unique molecular circuit whose attenuation transforms nonpolarized cells into polarized ones (Supplementary Fig. 1a,b). As the cascade terminates at the motor protein myosin II (further referred to as myosin), we

¹Department of Cell Biology, Harvard Medical School, 240 Longwood Avenue, Boston, Massachusetts 02115, USA. ²Department of Microbiology & Immunobiology, Harvard Medical School, 77 Avenue Louis Pasteur, Boston, Massachusetts 02115, USA. ³Department of Neurobiology, Physiology and Behavior, University of California, Davis, 1 Shields Avenue, Davis, California 95616, USA. ⁴Department of Mathematics, University of California, Davis, 1 Shields Avenue, Davis, California 95616, USA. ⁵National High Magnetic Field Laboratory and Department of Biological Science, Florida State University, 1800 E. Paul Dirac Drive, Tallahassee, Florida 32310, USA. ⁶These authors contributed equally to this work. ⁷Present addresses: Institut Curie, CNRS UMR 144, 26 rue d'Ulm, 75005 Paris, France (A.J.L.); Lyda Hill Department of Bioinformatics, UT Southwestern Medical Center, 5323 Harry Hines Boulevard, Dallas, Texas 75390-9039, USA (S.J.H. and G.D.); Courant Institute and Department of Biology, New York University, 251 Mercer Street, New York City, New York 10012, USA (K.-C.L. and A.M.).

⁸Correspondence should be addressed to A.M. or G.D. (e-mail: mogilner@cims.nyu.edu or Gaudenz.Danuser@UTSouthwestern.edu)

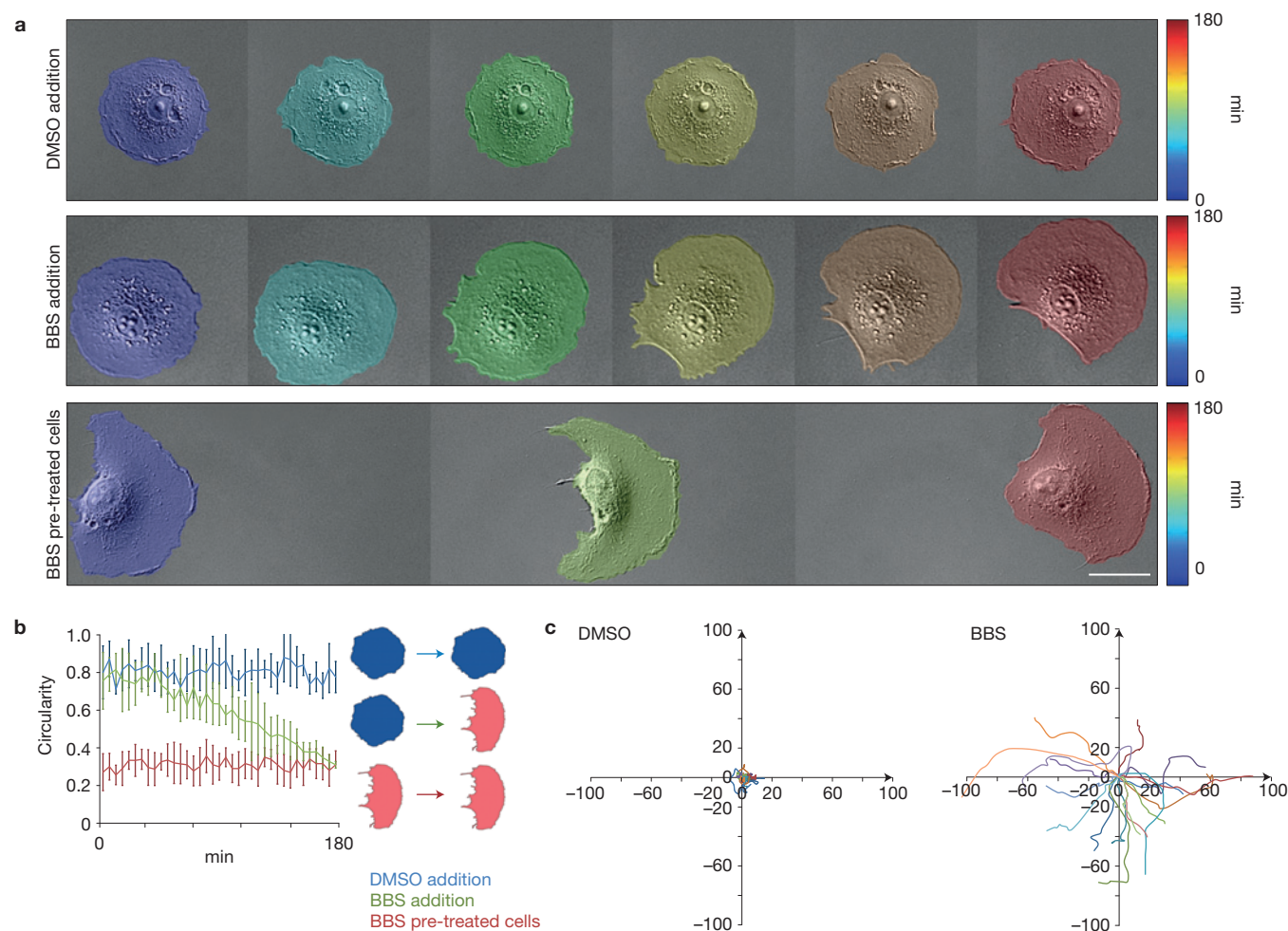


Figure 1 Acute inhibition of myosin II activity results in spontaneous symmetry breaking and motility initiation in single epithelial cells. (a) Representative video sequences of control cells (DMSO addition), cells after acute exposure to a myosin II inhibitor (BBS addition), and cells several hours after exposure to the inhibitor (BBS-pretreated cells). Scale bar, 20 μ m. (b) Cell shape circularity index (4π (area/perimeter²)) over time in single live cells at different experimental conditions. High circularity and its persistence over time is a morphodynamic signature of stationary, unpolarized cells. Low

circularity is a trait of migratory polarized cells. The decrease in the circularity index over time reflects a cell polarization event. Relatively large standard deviation for the circularity index over time in the BBS addition case is associated with an asynchrony of polarization events between individual cells on the same glass ($n=50$ cells per experimental condition; mean \pm s.d.). (c) Individual cells several hours after exposure to BBS exhibit markedly increased random migration. Trajectories of cell centroids (20 per condition) of DMSO- or BBS-pretreated cells tracked over 3 h are shown.

directly ablated its ATPase activity with the small-molecule drug blebbistatin (BBS, 25 μ M). When allowed to spread on a glass surface, IAR-2 cells assumed a discoid shape with almost perfect circular symmetry, which they maintained over hours (Fig. 1 and Supplementary Video 1). However, after addition of BBS, the cells underwent a spontaneous large-scale reorganization manifested in migratory polarization (Fig. 1a,b and Supplementary Fig. 1c,d and Supplementary Video 2): cells pushed their prospective front out and pulled in the back end, followed by initiation of persistent whole-cell migration (Fig. 1a–c and Supplementary Video 3). Polarization was stable in the presence of BBS (Fig. 1b, red curve), but cells switched back to their original, circularly symmetric shapes after wash out of BBS (Supplementary Fig. 2), indicating that myosin activity is the mediator of a reversible polarization switch.

Acute inhibition of RhoA and ROCK, but not other potentially involved molecular factors, produced a phenotypic response

remarkably similar to BBS treatment (Supplementary Fig. 1c,d), suggesting that myosin activity plays a decisive role in controlling large-scale morphodynamics of epithelial cells. To exclude nonspecific effects of the small-molecule inhibitors, we separately depleted by short interfering RNA (siRNA)-mediated gene silencing the two main isoforms of the myosin heavy chain, myosin IIA and myosin IIB. As partially expected from previous studies^{8,9}, knockdown of myosin IIA, but not of myosin IIB, resulted in the phenotype of epithelial cells treated with BBS (Supplementary Fig. 3a–d). Indeed, we succeeded in rescuing the myosin IIA deficiency phenotype in IAR-2 cells by ectopic expression of RNA-mediated interference (RNAi)-insensitive ATPase-competent wild-type myosin IIA, whereas expression of the RNAi-insensitive ATPase-defective mutant myosin IIA (N93K27; ref. 10) did not rescue the phenotype (Supplementary Fig. 3e). This rules out mechanisms other than myosin ATPase activity to control migratory polarization of epithelial cells, and justifies the use of the

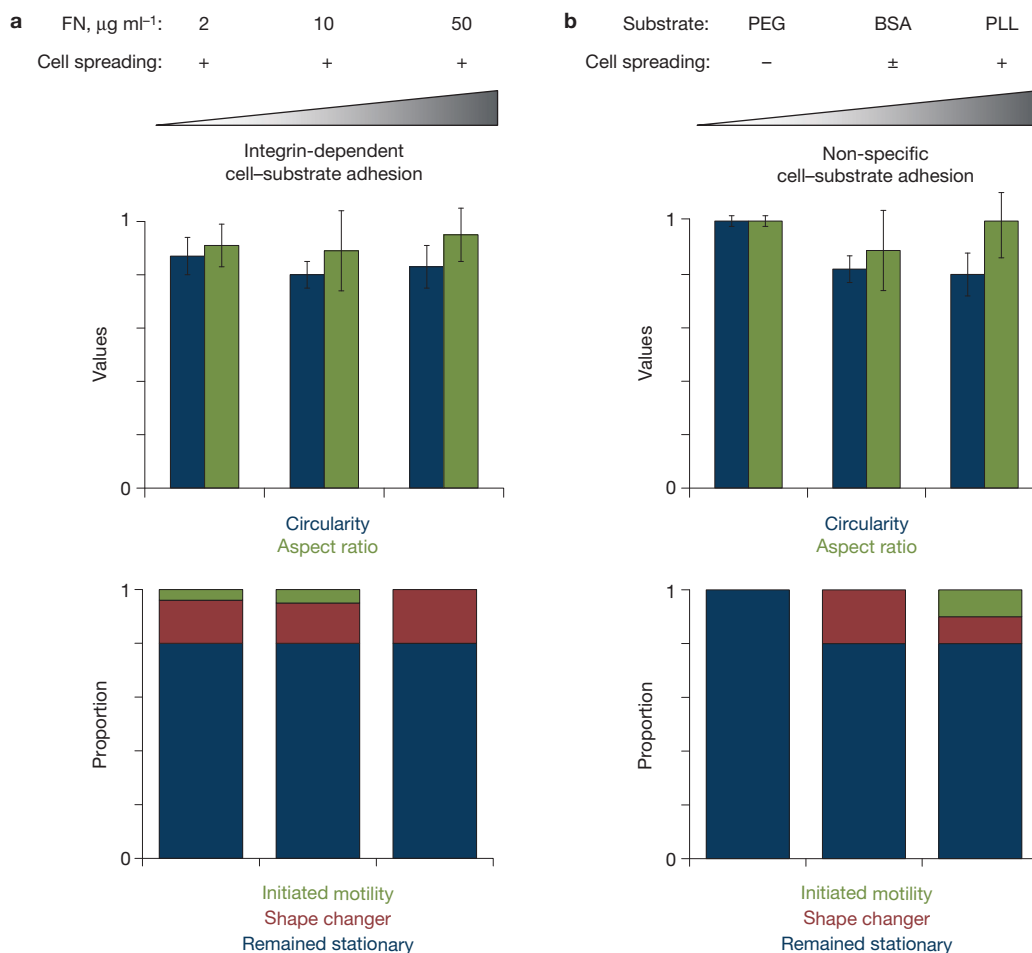


Figure 2 Modulating cell-substrate adhesion strength *per se* is insufficient to trigger spontaneous symmetry breaking and motility initiation in epithelial cells with intact myosin II activity. **(a)** Shape descriptors ($n=120$ cells per experimental condition; mean \pm s.e.m.; compared with DMSO-treated cells on glass (Supplementary Fig. 1c), P values for each of these conditions are >0.5 , two-tailed unpaired Student's t -test) and motility initiation frequency ($n=50$ cells per experimental condition) in pharmacologically untreated epithelial cells plated onto dishes pre-coated with fibronectin

(FN) at low ($2\mu\text{g ml}^{-1}$), intermediate ($10\mu\text{g ml}^{-1}$) or high ($50\mu\text{g ml}^{-1}$) concentrations. **(b)** Shape descriptors ($n=120$ cells per experimental condition; mean \pm s.e.m.; compared with DMSO-treated cells on glass (Supplementary Fig. 1c), P values for each of these conditions are >0.5 , two-tailed unpaired Student's t -test) and motility initiation frequency ($n=50$ cells per experimental condition) in pharmacologically untreated epithelial cells plated onto dishes pre-coated with 0.2 mg ml^{-1} polyethylene glycol (PEG), 50 mg ml^{-1} bovine serum albumin (BSA), or 1 mg ml^{-1} poly-L-lysine (PLL).

myosin ATPase inhibitor BBS as a specific tool to modulate migratory cell polarization.

Integrin-based substrate anchorage does not explain the inhibition of migratory cell polarization by myosin II in epithelial cells

Myosin activity promotes growth of integrin-based focal adhesions attaching cells to the extracellular matrix¹¹ (ECM). Strong anchorage of cells to ECM through focal adhesions renders cells immobile^{12,13}. At the same time, there are cases when cells can initiate motility after direct weakening of focal adhesions^{14,15}. We thus reasoned that myosin in epithelial cells prevents migratory cell polarization by facilitating strong focal-adhesion-mediated attachment to the ECM. However, our analyses of cell morphology as well as motility initiation frequency in cells plated on various adhesive and non-adhesive substrates did not support this hypothesis (Fig. 2), calling for an alternative explanation of myosin's effect on migratory cell polarization.

Sequestration of polymerization-competent actin in epithelial actin belts explains the inhibition of migratory cell polarization by myosin II

As myosin is an actin-based mechanochemical ATPase (ref. 11), we decided to investigate how the activity of myosin is coordinated with the actin cytoskeleton to regulate epithelial cell morphodynamics. Control cells accumulate most of their actin inside peripheral circumferential bundles (epithelial actin belt or ring), which is reflected in the extremely high ratio of F-actin fluorescence in the ring versus the cytoplasm (Fig. 3a). This subcellular distribution of actin mirrors that of active myosin (MRLC-Thr 18, Ser 19; ref. 16; Fig. 3b). Consistent with the spatial pattern of both proteins, we determined by laser ablation that actomyosin bundles within the ring are contractile (Supplementary Video 4). After laser ablation, F-actin in the peripheral actomyosin ring recovered with a mean half-time ($\tau_{1/2}$) of 3.0 min (s.e.m. = 0.4 min, $n=10$ cells), whereas F-actin in the cytoplasm recovered significantly faster (mean $\tau_{1/2}=10.2$ s,

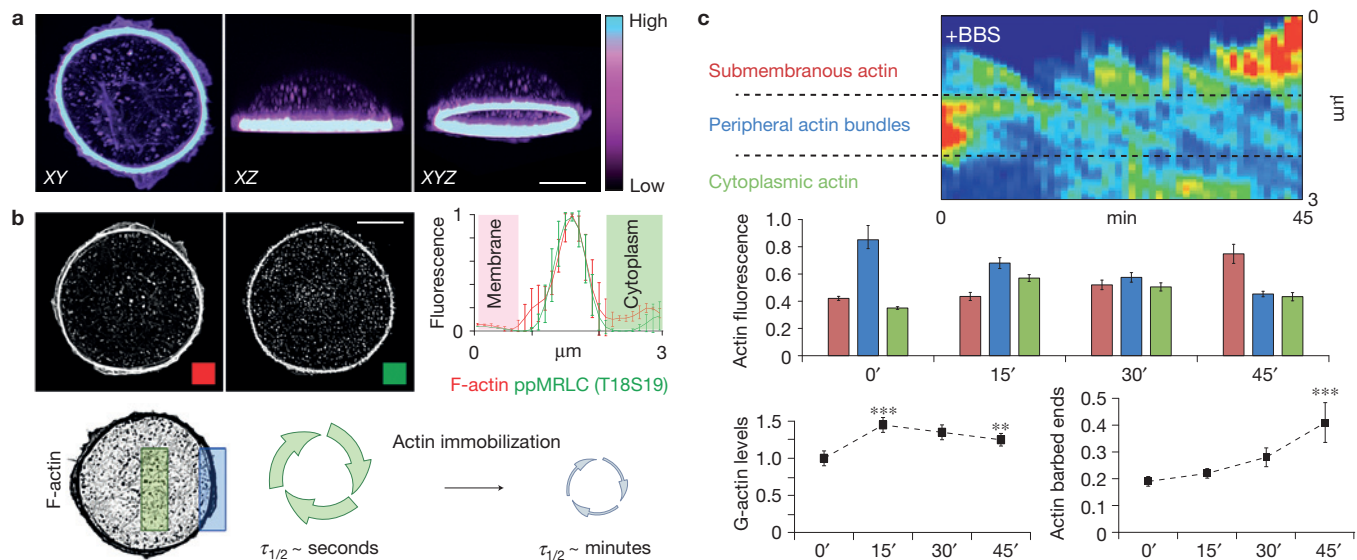


Figure 3 Myosin II activity suppresses actin polymerization at the cell edge by immobilizing actin inside peripheral actomyosin bundles. **(a)** Optical sectioning of a fixed stationary epithelial cell stained for F-actin (rhodamine-phalloidin). The colour scale indicates levels of F-actin fluorescence intensity. Scale bar, 10 μm . **(b)** Maximum intensity projections of F-actin and endogenous diphosphorylated myosin II regulatory light chain (ppMRLC (Thr 18/Ser 19)) in a fixed stationary epithelial cell. The linescan shows normalized average fluorescence intensity of F-actin (red) and diphosphorylated MRLC (green) along a profile (1 pixel across) pointing from the cell edge to the cytoplasm ($n=95$ cells; mean \pm s.e.m.). Both F-actin and diphosphorylated MRLC are concentrated in the cortical actin ring but largely absent from the cytoplasm, where actin turns over significantly faster compared with the cortical ring. Scale bar, 10 μm . **(c)** Dynamic redistribution pattern of actin at the cell periphery in response to acute inhibition of myosin II activity. Top, a representative kymograph and statistical analysis

($n=35$ cells; mean \pm s.e.m.) of local F-actin fluorescence (mCherry–Lifeact) intensity at the membrane, the actin ring, and the cytoplasm monitored in live cells immediately on addition of BBS. Hot colours on the kymograph represent high levels of F-actin fluorescence; cool colours are low F-actin fluorescence levels. Bottom left, retrospective analysis of endogenous cytoplasmic G-actin fluorescence levels (a.u., normalized values) at different time points after addition of BBS ($n=40$ cells per time point; mean \pm s.e.m.; *** $P < 0.001$ —comparison between 0' and 15' of BBS exposure, ** $P < 0.01$ —comparison between 15' and 45' of BBS exposure, two-tailed unpaired Student's t -test). Bottom right, fraction of submembranous actin barbed (growing) ends (fluorescence intensity ratio of newly incorporated actin monomers versus pre-existing actin polymer) at different time points after addition of BBS ($n=18$ cells per time point; mean \pm s.e.m.; *** $P < 0.001$ —comparison between 0' and 45' of BBS exposure, two-tailed unpaired Student's t -test).

s.e.m. = 0.9 s, $n=10$ cells; $P < 0.001$, paired samples t -test). However, peripheral F-actin recovered with the kinetics similar to that of cytoplasmic F-actin (mean $\tau_{1/2} = 10.0$, s.e.m. = 0.8 s, $n=12$ cells; $P > 0.5$, two-tailed unpaired Student's t -test) after inactivation of myosin with BBS, suggesting that myosin stabilizes actin inside the actomyosin ring.

Acute inhibition of myosin activity with BBS resulted in a reduced ratio of F-actin fluorescence at the cell edge versus the cytoplasm (Fig. 3c, top, first 15 min of exposure to the drug). These changes were paralleled by increased levels (1.5-fold change) of G-actin in the cytoplasm as visualized by DNase I staining^{17,18} (Fig. 3c, bottom left). The increase in G-actin levels indicated that F-actin stabilized in the actomyosin ring becomes available for turnover after myosin inhibition. At later stages (within ~ 40 min) of BBS treatment, the cells started accumulating F-actin at the cell edge (Fig. 3c, top), which was accompanied by a small but statistically significant decrease (1.25-fold change) in the levels of cytosolic G-actin (Fig. 3c, bottom left). The latter suggested that the G-actin released on turnover of F-actin from the actomyosin ring is recycled at the cell edge. Consistent with this conclusion, our experiments on G-actin incorporation *in situ*¹⁹ showed that BBS addition stimulates cells to engage more G-actin into actin networks at the cell edge over time (Fig. 3c, bottom right).

Collectively, these data showed that when myosin activity is suppressed, actin previously 'locked' inside the actomyosin ring

becomes available for deployment in the processes of actin assembly–disassembly–and–recycling typical for treadmilling actin arrays at the lamellipodium of migratory cells²⁰. These actin dynamics were crucial for driving migratory cell polarization after myosin inactivation, as pharmacological treatments to simultaneously stabilize F-actin and prevent incorporation of G-actin into the existing F-actin network (through application of a mixture of jasplakinolide and latrunculin, as described in ref. 21) in cells pretreated with BBS for 15 min entirely abrogate spontaneous cell polarization (100% of $n=35$ cells).

Myosin II-dependent actin immobilization inside peripheral actomyosin bundles suppresses autocatalytic growth of F-actin at the cell edge

At the ultrastructural level, the submembranous F-actin that enables lamellipodial protrusion in migratory polarized cells is known to be organized in a branched fashion^{22,23}. This spatial organization of F-actin is determined by the Arp2/3 protein complex that binds pre-existing growing actin filaments and stimulates the formation of new actin branches²², thus serving as a specific molecular marker of growing branched actin networks at the light microscope level. Accordingly, we found Arp2/3 primarily concentrated inside submembranous actin meshworks at the protrusive edge of myosin-inhibited cells, but not at the edge of control cells (Fig. 4a). We surmised that pre-existing submembranous actin networks in

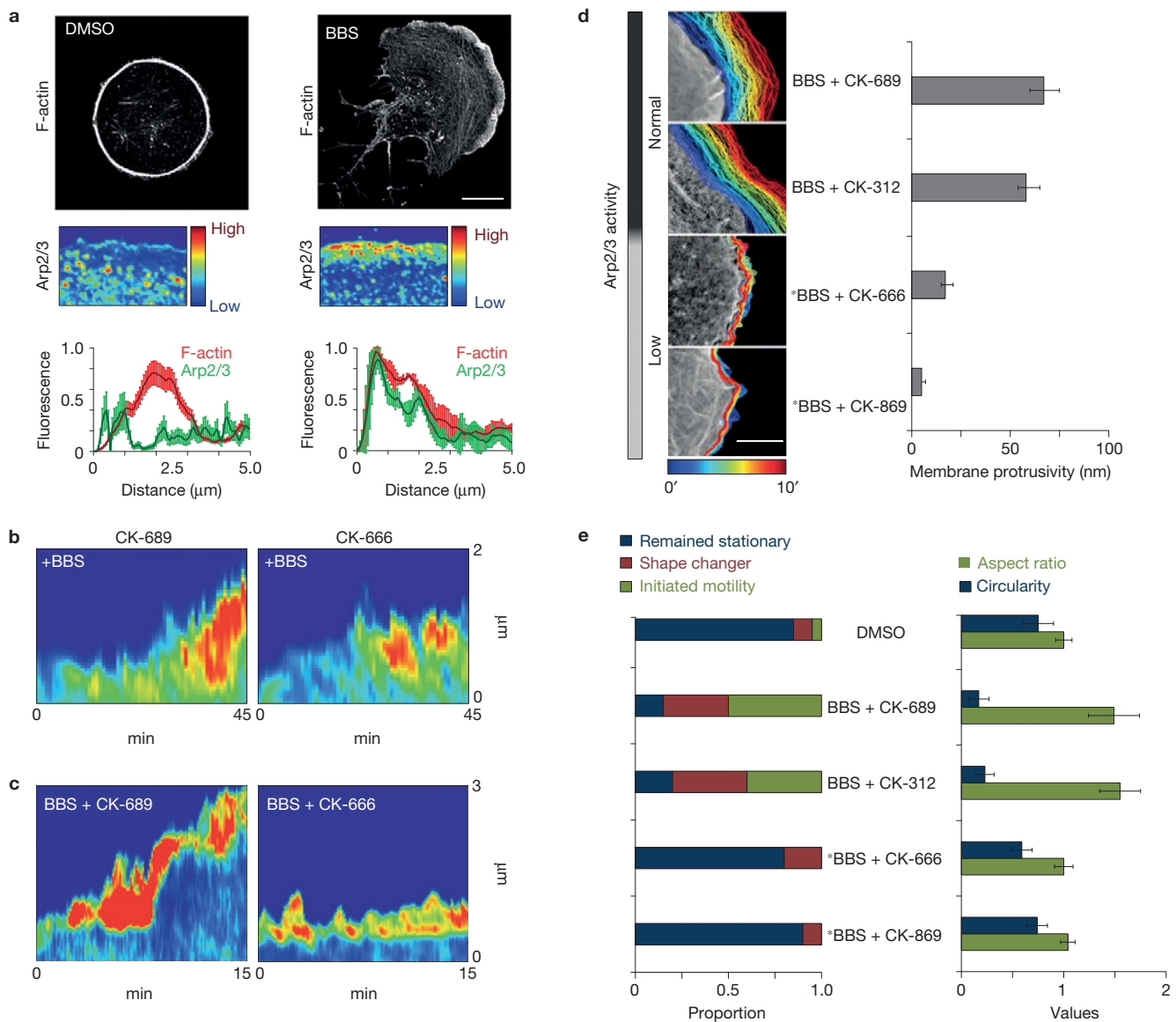


Figure 4 The growth of submembranous actin at the edge of myosin II-inhibited cells is strongly reinforced through Arp2/3-mediated F-actin branching. **(a)** Phalloidin staining (black and white images) and staining intensity of the cell edge by antibodies recognizing the Arp2 subunit of the Arp2/3 protein complex (pseudocoloured images with colour intensity scale bars) in cells treated with DMSO or BBS. Scale bar, $10\mu\text{m}$. Linescan, normalized average fluorescence intensity (a.u.) of F-actin and Arp2 along a line pointing from the cell edge to the cell centre ($n=50$ cells per experimental condition; mean \pm s.e.m.). **(b)** Representative kymographs of F-actin fluorescence (mCherry–Lifeact) intensity at the cell edge immediately on addition of BBS to cells pretreated with the nonspecific compound CK-689, or the Arp2/3-inhibiting compound CK-666. Hot colours on the kymograph represent high levels of F-actin fluorescence; cool colours are low F-actin fluorescence levels. **(c)** Representative kymographs of F-actin fluorescence (mCherry–Lifeact) intensity at the cell edge in cells pretreated with a mixture of BBS and the nonspecific compound CK-689, or BBS and

the Arp2/3-inhibiting compound CK-666 for several hours. Hot colours on the kymograph represent high levels of F-actin fluorescence; cool colours are low F-actin fluorescence levels. **(d)** Cell edge dynamics in cells co-treated with BBS and control, nonspecific compounds (CK-689 and CK-312), or BBS and Arp2/3-inhibiting compounds (CK-666 and CK-869) ($n=15$ cells per experimental condition; mean \pm s.e.m.; $*P<0.001$, two-tailed unpaired Student's *t*-test). The representative images of the cell edge dynamics show colour-coded outlines of the cell edge. Colour scale, time in minutes. Scale bar, $3\mu\text{m}$. **(e)** Left, motility initiation frequency of stationary cells within 4 h after addition of BBS and control, nonspecific compounds (CK-689 and CK-312), or BBS and Arp2/3-inhibiting compounds (CK-666 and CK-869) ($n=50$ cells per experimental condition). Right, shape descriptors measured in cells after 3 h of incubation with BBS and control, nonspecific compounds (CK-689 and CK-312), or BBS and Arp2/3-inhibiting compounds (CK-666 and CK-869) ($n=150$ cells per each experimental condition; mean \pm s.e.m.; $*P<0.001$, two-tailed unpaired Student's *t*-test).

myosin-inhibited cells start utilizing G-actin released on turnover of actin filaments previously stabilized inside the actomyosin ring. This allows the cells to nucleate more actin filaments at the emerging protrusive edge. The more actin filaments get engaged in the growth

at the membrane, the more surfaces will be offered for Arp2/3 to bind pre-existing actin filaments and stimulate the formation of new filaments, thus amplifying actin polymerization in an autocatalytic manner^{24,25}. In support of this, we observed that Arp2/3 is not

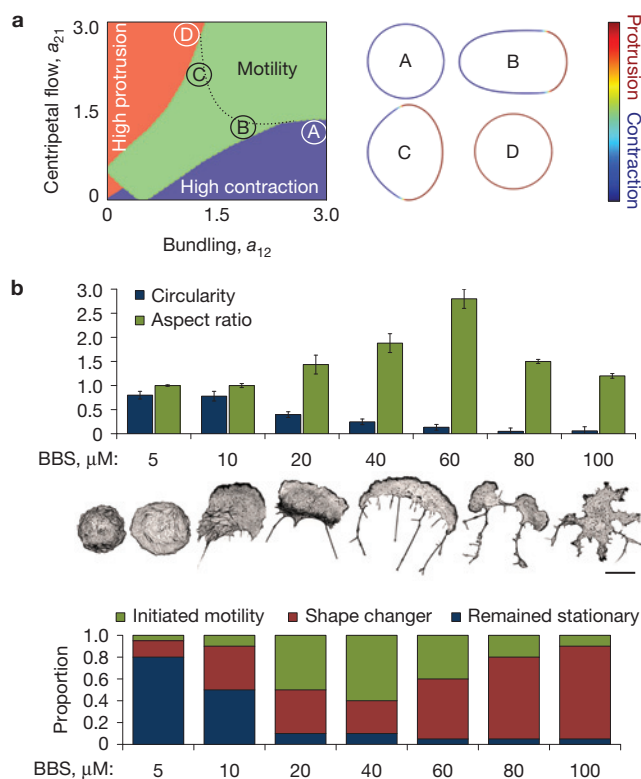


Figure 5 Mathematical model for migratory cell polarization based on the mass balance between actomyosin bundle formation and branched actin growth coupled to F-actin retrograde flow. **(a)** Motility phase diagram as a function of the bundling rate (a_{12}) and centripetal flow rate (a_{21}). The control cell corresponds to the high bundling rate (proportional to the myosin strength) and low centripetal flow rate (Cell A ($a_{12}=3$, $a_{21}=1.2$)). In this state, a constant high density of bundled actin develops around the periphery of the cell and the cell is symmetric. Inhibition of myosin (Cell B ($a_{12}=1.8$, $a_{21}=1.2$)) and enhanced centripetal flow rate (Cell C ($a_{12}=1.2$, $a_{21}=1.8$)) can cause the cell to polarize and move. Further inhibition of myosin and/or increasing centripetal flow rate can abolish cell movement and polarization. In this state (Cell D ($a_{12}=1.2$, $a_{21}=3$)), the bundled actin is nearly abolished and the branched actin is constant around the cell periphery creating a propulsive force that is balanced by membrane tension. The dotted line illustrates the path in the parameter space corresponding to gradual weakening of myosin. **(b)** Testing model predictions. Top, shape descriptors measured in cells after 3 h of incubation with increasing concentrations of BBS ($n=150$ cells per experimental condition; mean \pm s.e.m.). Images of the actin cytoskeleton represent phenotypes of cells treated with different BBS concentrations as indicated on the diagram. Bottom, motility initiation frequency of cells within 4 h after addition of BBS in different concentrations ($n=50$ cells per experimental condition). Scale bar, 20 μm .

essential for the initial actin enrichment at the plasma membrane seen after myosin downregulation (Fig. 4b). However, at later stages, Arp2/3 activity seemed to be crucial for a strong augmentation of the actin enrichment and its transformation into membrane protrusion (Fig. 4c). To examine whether the Arp2/3-dependent reinforcement of actin polymerization is implicated in the process of migratory polarization in myosin-inhibited cells, we co-treated cells with BBS and Arp2/3-inhibiting drugs. Such cells exhibited diminished membrane protrusivity and a low frequency of spontaneous cell shape polarization compared with cells treated with BBS and inactive control compounds (Fig. 4d,e). These observations suggest that Arp2/3-mediated branching of submembranous actin is required

to harness the increased pool of polymerization-competent actin for spontaneous symmetry breaking and motility initiation in myosin-inhibited cells.

A minimal model for migratory cell polarization

To link the established local mechanisms to global cell-scale morphodynamics, we developed a mathematical model (Supplementary Note), in which we consider cell shape and movement as functions of myosin strength that controls the balance between bundled and branched actin at the cell periphery. The model is based on the following theoretical assumptions and experimental observations: (1) Epithelial cells simultaneously assemble and maintain two major F-actin networks of different organization and dynamics—a small protruding band of branching filaments at the cell periphery and stationary contractile actomyosin bundles forming a cell-scale ring. (2) Consumption of actin by one F-actin network is critical to limit the amount of actin available for the other network²⁶. (3) The two actin networks are engaged in local mutual inhibition: (i) Peripheral actin gets immobilized inside actomyosin bundles with the rate proportional to myosin strength. (ii) Growth of the protruding actin filament network at the cell edge is expected to create effective local centripetal flow pushing the actomyosin bundles away from the edge. (4) Local movements of the cell edge affect the inhibitory crosstalk between the networks in two ways: (i) if the edge retracts, actomyosin bundles accumulate at the cell boundary compressing branched F-actin into bundles. (ii) If the edge protrudes, the growing branched filaments keep up with the edge but the actomyosin bundles lag behind. (5) Local network densities determine local cell edge dynamics: branched filaments push the edge outward, whereas contraction of circumferential bundles pulls the edge inward. The model has the features of a system that describes two species competing for the same resources²⁷. As the two actin networks locally compete for the same pool of actin, they cannot coexist. Rather, one ‘wins’ over the other to ultimately determine the degree of migratory cell polarity.

The model generated a phase diagram of cell migration phenotypes based on two control parameters: myosin-dependent rate at which actin gets immobilized in actomyosin bundles; and the rate at which the growing branched actin network locally propels the cell edge and transports actomyosin bundles away from the edge (Fig. 5a). This phase diagram predicted that cells polarize and initiate motility at an intermediary range of myosin activity (Fig. 5a, cells B to C, and Supplementary Video 5), whereas extreme myosin activity levels (too high or too low) produce nonpolarized cells deficient in migration. When myosin is fully activated, actin immobilization inside circumferential actomyosin bundles inhibits the membrane protrusion all around the cell periphery, resulting in a non-motile cell (Fig. 5a, cell A, Supplementary Fig. 4a, cell F, and Supplementary Video 6). With complete myosin inactivation, actin-based protrusions develop all around the cell and migration cannot be efficient owing to failure of such cells to form a single axis of polarity (Fig. 5a, cell D, Supplementary Fig. 4a, cell E, and Supplementary Video 7). Indeed, we established experimentally that BBS-treated cells polarize efficiently only in the presence of serum in the standard growth medium (Supplementary Fig. 5), which according to recent studies²⁸ is required to maintain basal levels of actomyosin contractility during cell transitions to amoeboid motility. This suggested that the

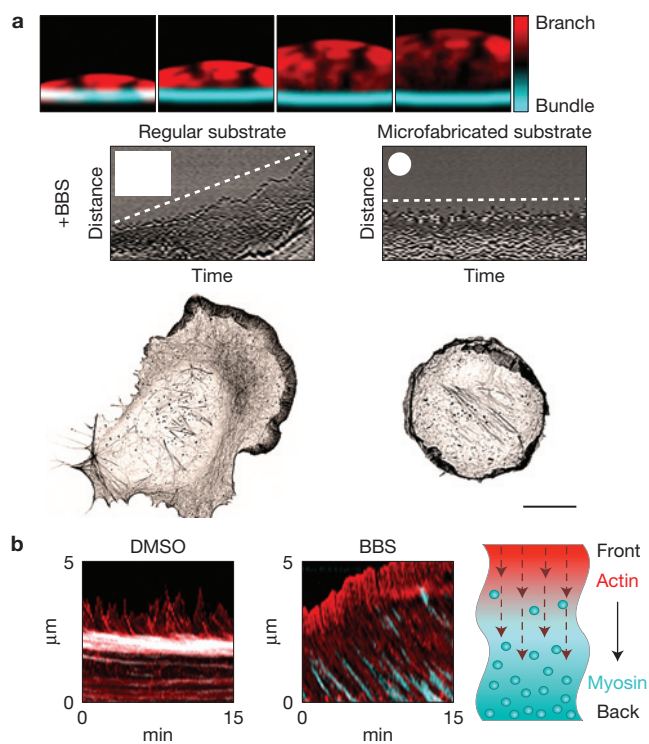


Figure 6 Low-contraction regimes enable spatial segregation among branched and bundled actin networks and facilitate actin–myosin flows. **(a)** Top, abstract representation of the spatial separation between branched and bundled actin populations in myosin-inhibited cells. Middle, representative kymographs of 1.5-h-long videos of cell edge dynamics after addition of BBS to cells plated on a regular glass surface versus microfabricated substrate. Bottom, representative images of F-actin distribution (maximum intensity projections) in BBS-pretreated (1.5 h of exposure to the drug) cells on a regular glass surface (left) versus cells plated on microfabricated substrates (right). Scale bar, 10 μm . **(b)** Representative kymographs of the edge of live cells expressing F-actin (red) and MRLC (cyan) and pretreated with DMSO or BBS for several hours. The cartoon depicts a possibility of myosin II's accumulation at the back of the cell by means of actin–myosin retrograde flows.

BBS concentration we use in our experiments inhibits actomyosin contractility partially, and a remaining myosin activity maintained by serum growth factors is essential for cell polarization. To test this in a more specific way, we modulated myosin activity with different concentrations of BBS at standard conditions (in the presence of serum). Our BBS dose–response experiments showed that both the degree of cell polarity and motility initiation frequency are insensitive to low concentrations of the drug (5–10 μM), but reach maximal values at an intermediate range of BBS concentrations (20–60 μM). High concentrations of the inhibitor (80–100 μM), which inactivate the cellular pool of myosin completely²⁹, decreased the frequency of motility initiation events. Such cells switched to irregular shapes by extending protrusions in different directions simultaneously, which precluded polarized cell movements (Fig. 5b). Thus, our experimental results are in agreement with predicted cell behaviours.

Spatial segregation among branched and bundled actin networks establishes cell-scale polarity

Our theoretical and experimental data suggested that untreated stationary cells possess relatively high basal levels of myosin activity

and that intermediary ranges of myosin activity are optimal for migratory cell polarization in this system. Stochastic simulations at intermediary ranges of myosin activity revealed that once actin bundling gets randomly suppressed along a significant part of the cell boundary, branched filaments at this part of the boundary will emerge and start pushing forward the cell membrane, leaving remnants of bundled filaments behind. This predicted that the local cell edge displacement should allow preferential accumulation of remaining actomyosin bundles behind the protrusive edge, thus establishing spatial asymmetries in the actin cytoskeleton (Fig. 6a and Supplementary Note). To test this mechanism, we decided to inhibit cell edge displacement without directly interfering with the growth of F-actin and see how it affects F-actin polarization triggered by partial myosin inactivation in cells. To suppress cell edge motion, we placed cells inside microfabricated cavities of a size and shape comparable to those of single cells (a circle with a diameter of 30 μm). In these conditions, cell edge displacement gets limited by the spatial constraints (Fig. 6a). BBS-treated cells on regular glass surfaces exhibited clear spatial separation between the branched actin mesh at the emerging front and remnants of actin bundles lagging behind during early stages of polarization (Fig. 6a). In contrast, cells grown within microfabricated substrates failed to separate branched and bundled actin populations; instead, branched actin starts growing all around the cell boundary, whereas remaining actin bundles get accumulated inside the cell (Fig. 6a). This supports the hypothesis that cell edge displacement is crucial for initial spatial separation of two distinct actin networks. In an alternative set of experiments, we inhibited cell motility by growing individual cells on circular micropatterns of fibronectin with a diameter of 40 μm , only 10 μm larger than the average cell size (\sim 30 μm). In these conditions, cells preserved the ability to change cell shape after myosin inhibition; however, they failed to generate stable asymmetry as their motility was restricted by the size of the adhesive micropattern (Supplementary Fig. 6), thus corroborating the model prediction.

Actin growth and retrograde flow transports myosin II to the back of the cell, maintaining a contractility gradient across the cell

Stochastic simulations showed that fluctuations in the density of actin, intrinsic to the process of actin polymerization, could easily disrupt the initial cell polarity established through the branch–bundle network separation mechanism. As our experiments demonstrate that myosin-inhibited cells can maintain their migratory polarity over time (Fig. 1b, red curve and Supplementary Video 3), some specific mechanisms should be in place to stabilize cell polarity. The F-actin network in motile cells often flows rearward as it polymerizes^{30,31}. In our experiments, we discovered that after partial myosin inhibition both F-actin and myosin start flowing from the cell front (Fig. 6b). Assuming that the flowing F-actin network transports myosin, but not the other way around, our simulations suggested that actin retrograde flow is a long-range inhibition mechanism (Fig. 6b and Supplementary Fig. 4e): the flow leads to myosin accumulation at the back, where the motor is crucial for contracting the actin network and thus limiting its growth.

In agreement with the theoretical predictions, our experiments showed that myosin-inhibited cells at initial stages of symmetry breaking exhibit centripetal flows of actin bundle remnants into the

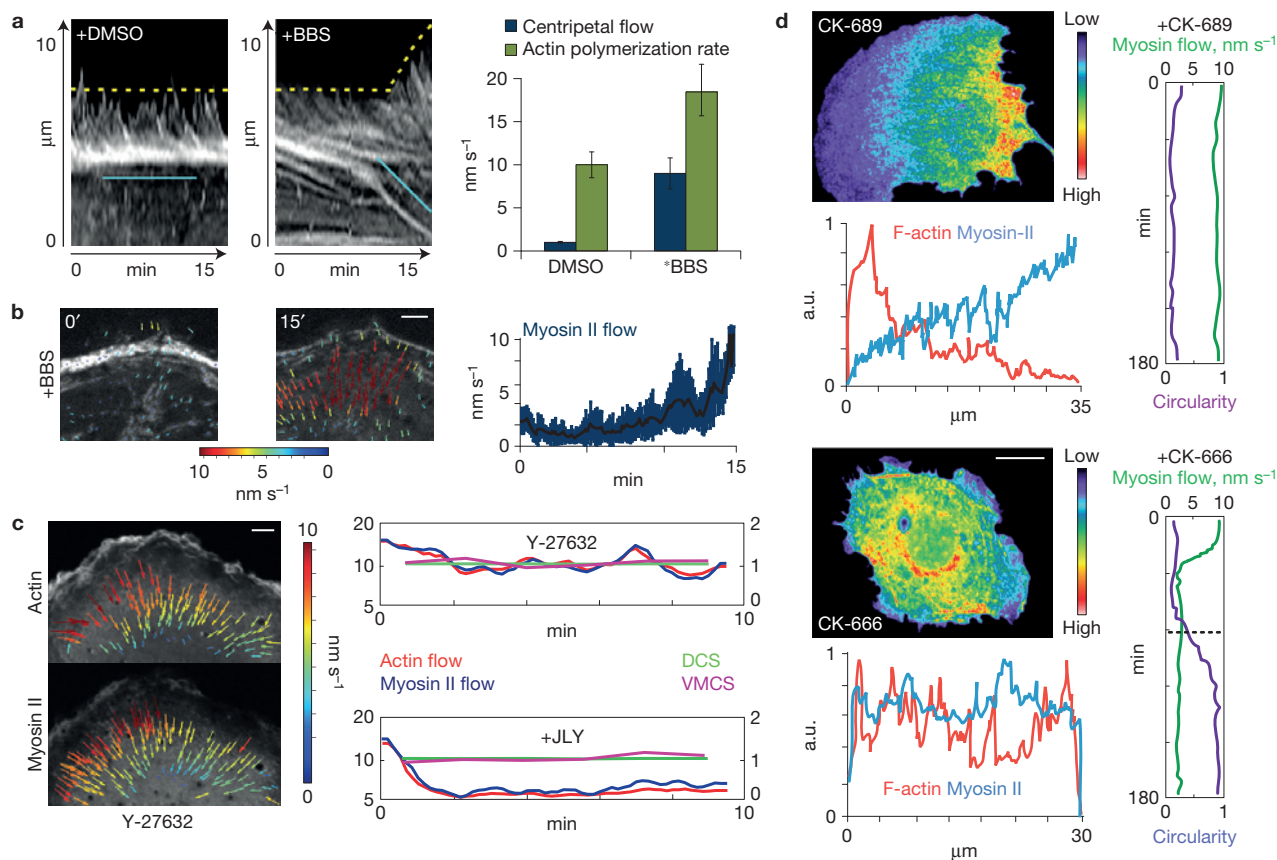


Figure 7 Experimental validation of model-predicted core motifs that compose the actin/myosin polarity-generating system. **(a)** Left, kymographs of F-actin dynamics after addition of DMSO or BBS (mCherry–LifeAct-expressing cells). Right, F-actin centripetal flows and actin polymerization rates ($n=20$ cells per condition; mean \pm s.e.m.; $*P < 0.001$, two-tailed unpaired Student's *t*-test). **(b)** Left, particle image velocimetry of myosin II clusters immediately after addition of BBS (mCherry–MRLC-expressing cells). Colour scale, flow velocity. Scale bar, $2\mu\text{m}$. Right, kinetics of myosin II retrograde flows after the addition of BBS ($n=10$ cells; mean \pm s.e.m.). **(c)** Retrograde flows of actin and myosin II quantified in Y-27632-treated cells, co-expressing GFP–MRLC and mCherry–LifeAct, before and after arresting the F-actin dynamics with a mixture of jasplakinolide and latrunculin on the background of Y-27632 (JLY) ($n=15$ cells per condition). DCS, direction coupling score, a measure of the directional similarities between F-actin and myosin II motions. VMCS, velocity magnitude coupling score, a measure of relative myosin II motion along the local F-actin flow axis, thus accounting for both

direction and speed. For identical flow fields, both DCS and VMCS are equal to 1. Colour scale, flow velocity. Scale bar, $2\mu\text{m}$. **(d)** Staining intensity by an antibody recognizing endogenous MRLC (pseudocoloured maximum intensity projections) in cells pretreated with BBS to induce polarity and subsequently exposed to either the nonspecific control compound CK-689 or the Arp2/3 inhibitor CK-666 for 2 h. Myosin II in myosin-inhibited cells treated with CK-689 is found at very low levels throughout the first $10\mu\text{m}$ of the cell front where most of retrograde actin–myosin flow is normally detected. Colour scale, staining intensity. Scale bar, $10\mu\text{m}$. Corresponding linescans, normalized average fluorescence intensity of F-actin (red) and MRLC (blue) along a line pointing from the front to the back of the cell. Kinetic profiles, mCherry–MRLC flow velocity (green) and cell shape circularity index (purple) measured at different time points in live cells pretreated with BBS to induce polarity and subsequently exposed to either CK-689 or CK-666 for 2 h. Black dotted line, a time point where cells start losing initial polarity.

cell interior and increased rates of actin polymerization (Fig. 7a) concomitant with the emergence of retrograde flows of myosin (Fig. 7b and Supplementary Video 8). These myosin flows persist in fully polarized migrating cells and are dependent on actin polymerization, as pharmacological treatments that stabilize the existing F-actin network and prevent new actin polymerization²¹ completely arrested the flows (Fig. 7c). The model predicts that myosin should move with the rate and direction similar to that of actin retrograde flow. We triggered cell polarization using Y-27632 and then applied correlational fluorescent speckle microscopy³² to confirm remarkably similar kinematics for actin and myosin flows (see quantification in Fig. 7c).

We further found that the passive rearward transport of myosin results in a front–back gradient of myosin concentrations across

the cell with the lowest levels of myosin at the front of the cell and the highest at the back (Fig. 7d). To determine whether this gradient of myosin distribution is indicative of spatial differences in contractility across the cell, we ablated the actin network with a pulsed laser beam at the front and the back of actomyosin-relaxed cells. Indeed, by comparing the recoil velocity of the cytoskeleton after laser cutting³³, we observed a fivefold increase in contractility from the front to the back (Supplementary Fig. 7). To equilibrate the spatial distribution of myosin across the cell and check how it affects cell polarity, we slowed down myosin flow by acutely inhibiting Arp2/3-dependent actin polymerization. In these conditions, cells started to gradually lose an asymmetric geometry, which is reflected in the increase of cell shape circularity index over time in most of the analysed cases (80%, $n=15$; Fig. 7d). Thus, local depletion of

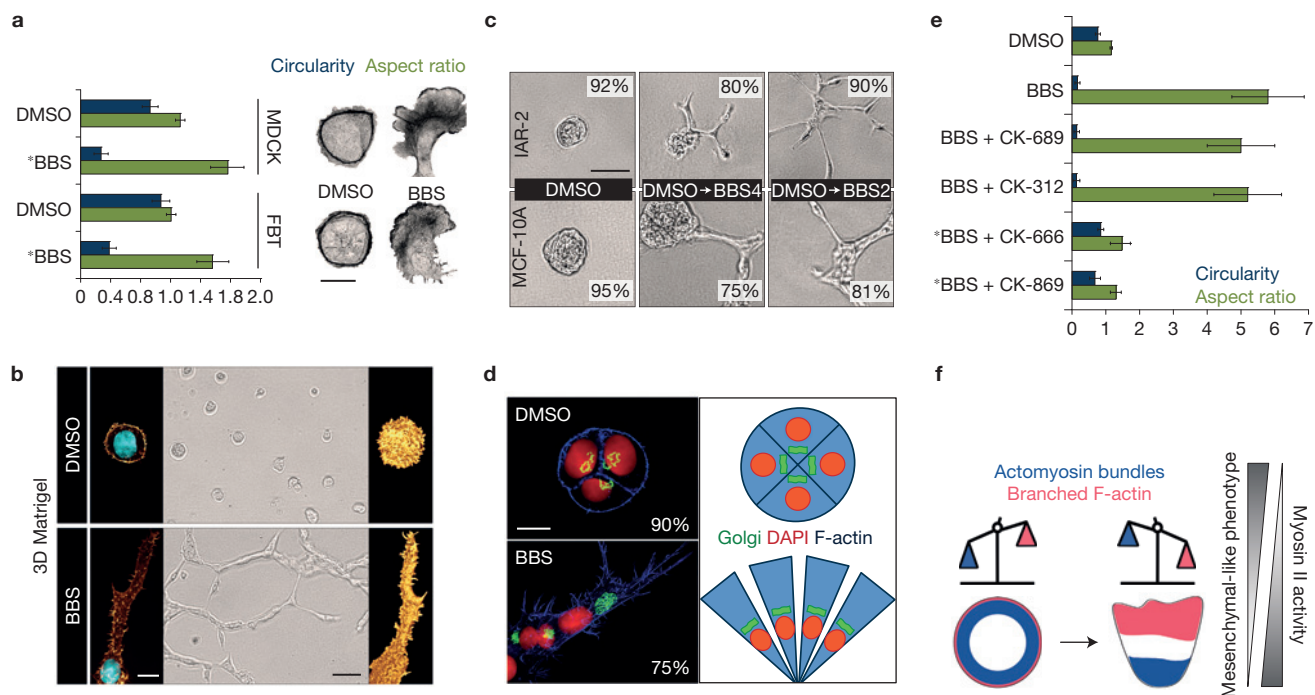


Figure 8 Testing generality of the actin/myosin polarity-generating mechanism in the context of epithelial biology. **(a)** Shape descriptors in MDCK-2 and FBT epithelial cells ($n=150$ cells per condition; mean \pm s.e.m.; $*P < 0.001$, two-tailed unpaired Student's t -test). Scale bar, $20\ \mu\text{m}$. **(b)** Left, nuclear and F-actin staining of single IAR-2 epithelial cells growing in 3D Matrigel. Scale bar, $10\ \mu\text{m}$. Middle, low-magnification phase-contrast images of single cells in 3D Matrigel. Scale bar, $30\ \mu\text{m}$. Right, 3D reconstruction of single-cell morphology based on optical sectioning of the entire cell volume by confocal microscopy. DMSO, control; BBS, myosin II inactivation. **(c)** Multicellular spheroid morphogenesis in IAR-2 and MCF-10A epithelial cells growing in 3D Matrigel: DMSO, 4-day-old spheroids treated with DMSO for 24 h; DMSO \rightarrow BBS4, 3-day-old spheroids were treated with DMSO for 24 h, and on day 4 the medium was changed and BBS was added for 24 h; DMSO \rightarrow BBS2, 1-day-old spheroids, consisting of 2 to 4 cells, were treated with DMSO for 24 h, and on day 2 the medium was changed and BBS was added for 48 h. Percentage of spheroids with

representative morphologies (phase-contrast images) is indicated; $n=250$ spheroids for each data point. Scale bar, $50\ \mu\text{m}$. **(d)** Internal polarity of individual IAR-2 cells within spheroids assembled in 3D Matrigel. Confocal medial slices of F-actin and the nucleus, as well as maximum intensity projections of the Golgi apparatus, are shown. Percentage of cells with inward (\leftarrow) and outward (\rightarrow) Golgi localization is indicated on images for DMSO and BBS treatment case, respectively; $n=150$ cells for each data point. Scale bar, $10\ \mu\text{m}$. **(e)** Shape descriptors in IAR-2 cells growing in 3D Matrigel and treated with BBS, BBS and nonspecific compounds, or BBS and Arp2/3-inhibiting drugs ($n=180$ cells per condition; mean \pm s.e.m.; $*P < 0.001$, two-tailed unpaired Student's t -test). **(f)** A simplified model. Stationary epithelial cells can be transformed into mesenchymal-like cells after lowering levels of actomyosin contractility. Under low-contraction regimes, the balance between Arp2/3- and myosin-dependent actin networks is shifted towards the growth of branched F-actin crucial for lamellipodial motility.

myosin from the leading edge by actin retrograde flows reinforces global front-back asymmetry. When we examined F-actin structure and dynamics in Arp2/3-inhibited cells after BBS treatment, we found that such cells assemble linear actin cables throughout the entire cell periphery (Supplementary Fig. 8). Previous reports show that this F-actin pattern emerges in Arp2/3-inactivated cells owing to random formation of peripheral actin cables by formins at the expense of Arp2/3-dependent branched actin meshworks normally focused at the leading cell edge^{26,34,35}. Thus, in addition to the mechanisms we describe in this work, spatial restriction of actin assembly by different actin-nucleating factors could impact cell polarization.

The role of reduced contractility in epithelial biology

To test the generality of the proposed model, we first partially inactivated myosin in two other epithelial cell lines (canine kidney (MDCK-2) and fetal bovine tracheal (FBT) epithelial cells). These cells, similar to IAR-2 epithelial cells, exhibit peripheral actomyosin rings. After treatment with BBS ($25\ \mu\text{M}$), MDCK-2 and FBT cells lost their actomyosin rings and acquired migratory polarized

shapes with distinctive actin mesh-rich pseudopodia at the front (Fig. 8a), therefore confirming the phenotype of myosin-inhibited IAR-2 cells (Fig. 1a and Fig. 4a). Next, we tested whether epithelial cell shape polarization takes place in conditions that physically and chemically mimic *in vivo* epithelial microenvironments. We cultured IAR-2 cells within three-dimensional (3D) Matrigel basement membrane matrices. The cells grown in control conditions exhibited perfectly symmetric spherical morphology (Fig. 8b). However, myosin inhibition in these cells resulted in an invasive phenotype exhibiting cell dissemination into the basement membrane matrix. Such cells acquired elongated shapes with pronounced actin-filled protrusions and inverted orientation of epithelial polarity, such that the Golgi apparatus becomes misoriented towards the basement membrane matrix, which is a distinctive feature of motile mesenchymal cells exhibiting anteroposterior polarity^{36,37} (Fig. 8b–d). A similar behaviour was observed in a classical model of epithelial 3D morphogenesis, non-tumorigenic human mammary gland epithelial cells (MCF-10A; Fig. 8c). To examine whether the epithelial cell shape polarization phenotype in three dimensions is also dependent on

branched polymerization of actin filaments, we co-treated myosin-inactivated IAR-2 cells growing in 3D matrices with Arp2/3-inhibiting drugs. We found that the elongated invasive morphology of myosin-inhibited cells was strongly dependent on Arp2/3-mediated branched polymerization of F-actin (Fig. 8e). Thus, we established that actomyosin contractility restrains migratory polarization of epithelial cells in 3D microenvironments, and that shifting the balance between actin bundling and branching is sufficient to trigger transitions between discrete cell shapes both in 2D and 3D conditions (Fig. 8f).

DISCUSSION

Competition for a limiting resource is most commonly associated with ecological communities³⁸. However, recent works demonstrate that competitive interactions also apply at the molecular level inside a living cell. It has been shown that Arp2/3-mediated F-actin meshworks compete for G-actin with formin- or Ena/VASP-assembled actin polymers to regulate the size and structure of the bulk F-actin cytoskeleton in both fission yeast and animal tissue cells^{26,39,40}. Our findings provide a functional application for similar processes, in which competition among Arp2/3- and myosin-dependent F-actin networks defines a mechanism for cell polarization and motility initiation. At the core of this mechanism is the ability of the actin-based motor myosin II to immobilize actin inside cortical actomyosin bundles and thus make it unavailable for deployment in the process of dendritic growth. We show that non-tumorigenic epithelial cells are inherently motile and rely on the dendritic actin growth at the cell edge to propel themselves; however, this property is normally inhibited by myosin activity. This is because the actin machinery in epithelial cells engages primarily in the assembly of contractile actomyosin bundles and is thus unavailable to form polarized protrusions required for motility. The key for the proposed mechanism to work is the ability of myosin to stabilize actin in contractile actomyosin structures, which is consistent with results of previous functional and biochemical studies^{41–45}. Furthermore, different types of non-motile or slow-moving cell are known to exhibit a large pool of stabilized F-actin, whereas fast-moving cells are characterized by significantly enhanced F-actin turnover rates and a lower pool of stable F-actin⁴⁶. The mechanism might explain why direct or indirect myosin II inactivation stimulates the formation of polarized actin-rich protrusions and promotes cell migration in a variety of cell types and experimental settings^{8,9,47–51}.

To reach and colonize a distant place in the organism, epithelial cells in a developing embryo or during carcinogenesis employ a large arsenal of migration modes^{52,53}. Recent work on various cell types has identified specific mechanisms and conditions required for myosin-dependent polarization and amoeboid motility when cells are in the high-contractility mode^{15,28}. Our research explores the other end of the spectrum—low-contractility regimes—and contributes to the understanding of the intrinsic mechanisms behind transitions of epithelial cells to mesenchymal-like phenotypes. We found that decreasing contractility below a critical threshold level of myosin activity is sufficient to switch epithelial cells from a stationary nonpolarized mode to a stably polarized migratory state. We show that this stable polarization is maintained by the autocatalytic growth of the branched actin network at the front and by a long-range crosstalk from the front to the back in which continuous membrane protrusion at the

front produces actin retrograde flow, transporting myosin to the back. Consistent with these observations, recent findings demonstrate that the actin flow-driven assembly of stable myosin gradients across the cell is a generic property of cells undergoing polarized migration⁵⁴. We demonstrate that the transition of epithelial cells to a stably polarized migratory state is reversible. These data coupled to our minimal mathematical model suggest that the observed transition does not require an elaborate genetic program, but rather occurs as a simple mechanical switch triggered by decreased contractility. As levels of myosin-dependent contractility are reversibly modulated by physico-chemical properties of the extracellular environment¹¹, cells *in vivo* can utilize the myosin-dependent switch to choose between different morphodynamic modes depending on environmental conditions. □

METHODS

Methods and any associated references are available in the [online version of the paper](#).

Note: Supplementary Information is available in the online version of the paper

ACKNOWLEDGEMENTS

The authors wish to acknowledge E. Bonder (Rutgers University, Newark, New Jersey, USA), T. Omelchenko (Sloan-Kettering Institute, New York, New York, USA) and J. Vasiliev (National Cancer Research Center, Moscow, Russia) for providing epithelial cell lines. We are grateful to I. Ethell (University of California Riverside, California, USA), S. Narumiya (Kyoto University, Japan), K. Kaibuchi (Nagoya University, Japan) and R. Horwitz (University of Virginia, Charlottesville, Virginia, USA) for sharing genetic constructs. We also thank M. Piel (Institut Curie, Paris, France) and D. Bonazzi (Institut Pasteur, Paris, France) for comments on the manuscript. This research was supported by a postdoctoral fellowship from the Leukemia & Lymphoma Society (grant no. 5388-13) to A.J.L., and the National Institutes of Health grants R01 GM071868 to G.D. and GM068952 to A.M. All light microscopy experiments described in the present work were performed at the Nikon Imaging Center of Harvard Medical School, Boston, Massachusetts.

AUTHOR CONTRIBUTIONS

A.J.L., K.-C.L., A.M. and G.D. designed the project. A.J.L. and K.-C.L. performed all key experiments and analysed the data. D.A.B. performed 3D experiments. S.J.H. developed the software for membrane protrusivity and myosin flow analyses. M.D. generated fluorescence reporters for live-cell imaging experiments. A.J.L., A.M. and G.D. wrote the manuscript. All authors discussed the results and implications, and commented on the manuscript at all stages.

COMPETING FINANCIAL INTERESTS

The authors declare no competing financial interests.

Published online at <http://dx.doi.org/10.1038/ncb3246>

Reprints and permissions information is available online at www.nature.com/reprints

- Nieto, M. A. Epithelial plasticity: a common theme in embryonic and cancer cells. *Science* **342**, 1234850 (2013).
- Muthuswamy, S. K. & Xue, B. Cell polarity as a regulator of cancer cell behavior plasticity. *Annu. Rev. Cell Dev. Biol.* **28**, 599–625 (2012).
- Hall, A. Rho GTPases and the actin cytoskeleton. *Science* **279**, 509–514 (1998).
- Bakal, C., Aach, J., Church, G. & Perrimon, N. Quantitative morphological signatures define local signaling networks regulating cell morphology. *Science* **316**, 1753–1756 (2007).
- Sahai, E. & Marshall, C. J. Differing modes of tumour cell invasion have distinct requirements for Rho/ROCK signalling and extracellular proteolysis. *Nat. Cell Biol.* **8**, 711–719 (2003).
- Sanz-Moreno, V. *et al.* Rac activation and inactivation control plasticity of tumor cell movement. *Cell* **135**, 510–523 (2008).
- Croft, D. R. & Olson, M. F. Regulating the conversion between rounded and elongated modes of cancer cell movement. *Cancer Cell* **14**, 349–351 (2008).
- Even-Ram, S. *et al.* Myosin IIA regulates cell motility and actomyosin-microtubule crosstalk. *Nat. Cell Biol.* **3**, 299–309 (2007).
- Schramek, D. *et al.* Direct *in vivo* RNAi screen unveils myosin IIA as a tumor suppressor of squamous cell carcinomas. *Science* **343**, 309–313 (2014).
- Vicente-Manzanares, M., Zareno, J., Whitmore, L., Choi, C. K. & Horwitz, A. F. Regulation of protrusion, adhesion dynamics, and polarity by myosins IIA and IIB in migrating cells. *J. Cell Biol.* **176**, 573–580 (2007).

11. Vicente-Manzanares, M., Ma, X., Adelstein, R. S. & Horwitz, A. R. Non-muscle myosin II takes centre stage in cell adhesion and migration. *Nat. Rev. Mol. Cell Biol.* **10**, 778–790 (2009).
12. Gupton, S. L. & Waterman-Storer, C. M. Spatiotemporal feedback between actomyosin and focal-adhesion systems optimizes rapid cell migration. *Cell* **125**, 1361–1374 (2006).
13. Wu, X., Kodama, A. & Fuchs, E. ACF7 regulates cytoskeletal-focal adhesion dynamics and migration and has ATPase activity. *Cell* **135**, 137–148 (2008).
14. Barnhart, E., Lee, K. C., Allen, G. M., Theriot, J. A. & Mogilner, A. Balance between cell-substrate adhesion and myosin contraction determines the frequency of motility initiation in fish keratocytes. *Proc. Natl Acad. Sci. USA* **112**, 5045–5050 (2015).
15. Liu, Y. J. *et al.* Confinement and low adhesion induce fast amoeboid migration of slow mesenchymal cells. *Cell* **160**, 659–672 (2015).
16. Watanabe, T., Hosoya, H. & Yonemura, S. Regulation of myosin II dynamics by phosphorylation and dephosphorylation of its light chain in epithelial cells. *Mol. Biol. Cell* **18**, 605–616 (2007).
17. Cramer, L. P., Briggs, L. J. & Dawe, H. R. Use of fluorescently labelled deoxyribonuclease I to spatially measure G-actin levels in migrating and non-migrating cells. *Cell Motil. Cytoskeleton* **51**, 27–38 (2002).
18. Connelly, J. T. *et al.* Actin and serum response factor transduce physical cues from the microenvironment to regulate epidermal stem cell fate decisions. *Nat. Cell Biol.* **12**, 711–718 (2010).
19. Symons, M. H. & Mitchison, T. J. Control of actin polymerization in live and permeabilized fibroblasts. *J. Cell Biol.* **114**, 503–513 (1991).
20. Pollard, T. D., Blanchoin, L. & Mullins, R. D. Actin dynamics. *J. Cell Sci.* **114**, 3–4 (2001).
21. Peng, G. E., Wilson, S. R. & Weiner, O. D. A pharmacological cocktail for arresting actin dynamics in living cells. *Mol. Biol. Cell* **22**, 3986–3994 (2011).
22. Mullins, R. D., Heuser, J. A. & Pollard, T. D. The interaction of Arp2/3 complex with actin: nucleation, high affinity pointed end capping, and formation of branching networks of filaments. *Proc. Natl Acad. Sci. USA* **95**, 6181–6186 (1998).
23. Yang, C. & Svitkina, T. Visualizing branched actin filaments in lamellipodia by electron tomography. *Nat. Cell Biol.* **13**, 1012–1013 (2011).
24. Sambeth, R. & Baumgaertner, A. Autocatalytic polymerization generates persistent random walk of crawling cells. *Phys. Rev. Lett.* **86**, 5196–5199 (2001).
25. Carlsson, A. E. Dendritic actin filament nucleation causes traveling waves and patches. *Phys. Rev. Lett.* **104**, 228102 (2010).
26. Burke, T. A. *et al.* Homeostatic actin cytoskeleton networks are regulated by assembly factor competition for monomers. *Curr. Biol.* **24**, 579–585 (2014).
27. Edelstein-Keshet, L. *Mathematical Models in Biology* (SIAM, 2005).
28. Ruprecht, V. *et al.* Cortical contractility triggers a stochastic switch to fast amoeboid cell motility. *Cell* **160**, 673–685 (2015).
29. Shutova, M., Yang, C., Vasiliev, J. M. & Svitkina, T. Functions of nonmuscle myosin II in assembly of the cellular contractile system. *PLoS ONE* **7**, e40814 (2012).
30. Henson, J. H. *et al.* Two components of actin-based retrograde flow in sea urchin ctenophores. *Mol. Biol. Cell* **10**, 4075–4090 (1999).
31. Ponti, A., Machacek, M., Gupton, S. L., Waterman-Storer, C. M. & Danuser, G. Two distinct actin networks drive the protrusion of migrating cells. *Science* **305**, 1782–1786 (2004).
32. Hu, K., Ji, L., Applegate, K. T., Danuser, G. & Waterman-Storer, C. M. Differential transmission of actin motion within focal adhesions. *Science* **315**, 111–115 (2007).
33. Mayer, M., Depken, M., Bois, J. S., Jülicher, F. & Grill, S. W. Anisotropies in cortical tension reveal the physical basis of polarizing cortical flows. *Nature* **467**, 617–621 (2010).
34. Koestler, S. A. *et al.* Arp2/3 complex is essential for actin network treadmilling as well as for targeting of capping protein and cofilin. *Mol. Biol. Cell* **24**, 2861–2875 (2012).
35. Henson, J. H. *et al.* Arp2/3 complex inhibition radically alters lamellipodial actin architecture, suspended cell shape, and the cell spreading process. *Mol. Biol. Cell* **26**, 887–900 (2015).
36. Kupfer, A., Louvard, D. & Singer, S. J. Polarization of the Golgi apparatus and the microtubule-organizing center in cultured fibroblasts at the edge of an experimental wound. *Proc. Natl Acad. Sci. USA* **79**, 2603–2607 (1982).
37. Bryant, D. M. & Mostov, K. E. From cells to organs: building polarized tissue. *Nat. Rev. Mol. Cell Biol.* **9**, 887–901 (2008).
38. Gause, G. F. *The Struggle for Existence* (Williams & Wilkins, 1934).
39. Suarez, C. *et al.* Profilin regulates F-actin network homeostasis by favoring formin over Arp2/3 complex. *Dev. Cell* **32**, 43–53 (2015).
40. Rotty, J. D. *et al.* Profilin-1 serves as a gatekeeper for actin assembly by Arp2/3-dependent and -independent pathways. *Dev. Cell* **32**, 54–67 (2015).
41. Engl, W., Arasi, B., Yap, L. L., Thiery, J. P. & Viasnoff, V. Actin dynamics modulate mechanosensitive immobilization of E-cadherin at adherens junctions. *Nat. Cell Biol.* **16**, 587–594 (2014).
42. Wu, S. K. *et al.* Cortical F-actin stabilization generates apical-lateral patterns of junctional contractility that integrate cells into epithelia. *Nat. Cell Biol.* **16**, 167–178 (2014).
43. Wiggan, O., Shaw, A. E., DeLuca, J. G. & Bamberg, J. R. ADF/cofilin regulates actomyosin assembly through competitive inhibition of myosin II binding to F-actin. *Dev. Cell* **22**, 530–543 (2012).
44. Elam, W. A., Kang, H. & De La Cruz, E. M. Competitive displacement of cofilin can promote actin filament severing. *Biochem. Biophys. Res. Commun.* **438**, 728–731 (2013).
45. Hayakawa, K., Tatsumi, H. & Sokabe, M. Actin filaments function as a tension sensor by tension-dependent binding of cofilin to the filament. *J. Cell Biol.* **195**, 721–727 (2011).
46. McGrath, J. L., Osborn, E. A., Tardy, Y. S., Dewey, C. F. Jr & Hartwig, J. H. Regulation of the actin cycle *in vivo* by actin filament severing. *Proc. Natl Acad. Sci. USA* **97**, 6532–6537 (2000).
47. Omelchenko, T., Vasiliev, J. M., Gelfand, I. M., Feder, H. H. & Bonder, E. M. Mechanisms of polarization of the shape of fibroblasts and epitheliocytes: separation of the roles of microtubules and Rho-dependent actin-myosin contractility. *Proc. Natl Acad. Sci. USA* **99**, 10452–10457 (2002).
48. Omelchenko, T., Vasiliev, J. M., Gelfand, I. M., Feder, H. H. & Bonder, E. M. Rho-dependent formation of epithelial “leader” cells during wound healing. *Proc. Natl Acad. Sci. USA* **100**, 10788–10793 (2003).
49. Wang, H. R. *et al.* Regulation of cell polarity and protrusion formation by targeting RhoA for degradation. *Science* **302**, 1775–1779 (2003).
50. Asokan, S. B. *et al.* Mesenchymal chemotaxis requires selective inactivation of myosin II at the leading edge via a noncanonical PLC γ /PKC α pathway. *Dev. Cell* **31**, 747–760 (2014).
51. Lou, S. S., Diz-Muñoz, A., Weiner, O. D., Fletcher, D. A. & Theriot, J. A. Myosin light chain kinase regulates cell polarization independently of membrane tension or Rho kinase. *J. Cell Biol.* **209**, 275–288 (2015).
52. Lämmermann, T. & Sixt, M. Mechanical modes of ‘amoeboid’ cell migration. *Curr. Opin. Cell Biol.* **21**, 636–644 (2009).
53. Friedl, P. & Alexander, S. Cancer invasion and the microenvironment: plasticity and reciprocity. *Cell* **147**, 992–1009 (2011).
54. Maiuri, P. *et al.* Actin flows mediate a universal coupling between cell speed and cell persistence. *Cell* **161**, 374–386 (2015).

METHODS

Cell culture. Normal rat liver (IAR-2) and fetal bovine tracheal (FBT) epithelial cells were provided by E. Bonder (Rutgers University, Newark, New Jersey, USA) and T. Omelchenko (Sloan-Kettering Institute, New York, New York, USA). Normal canine kidney (MDCK-2) epithelial cells were purchased from American Type Culture Collection (ATCC). Cell lines were authenticated by STR profiling at ATCC and tested for mycoplasma contamination using the MycoScope PCR Mycoplasma Detection Kit (Genlantis). Cells were maintained in DMEM/F12 supplemented with 10% FBS (Invitrogen) at 37 °C and 5% CO₂. For experiments, cells were plated at a low confluence (10–20%) on 22 × 22-mm No. 1.5 acid-washed coverslips with no pre-coating for 24 h before experimental manipulations. In the experiments for Supplementary Fig. 4, cells were plated on plasma-treated glass coverslips coated with either fibronectin (Millipore), poly-L-lysine (Merck KGaA), BSA (Sigma-Aldrich), or poly-L-lysine-PEG copolymer (SuSoS AG).

Transfection procedure, expression vectors, and siRNA oligonucleotides. Cells were transfected with plasmid DNA using Lipofectamine LTX reagent (Invitrogen) transiently or stably, according to the manufacturer's protocol. For RNA interference experiments, cells were transfected with siRNA oligonucleotides using Lipofectamine RNAiMAX reagent (Invitrogen), according to the manufacturer's protocol.

The following expression vectors were used for plasmid DNA transfections: empty vector pEGFP-C1 (Clontech); pCMX-myc-p160^{ROCK} (wt) and pCMX-myc-p160^{ROCK} (kinase-dead/kd) (ref. 55); pcDNA3-EGFP-cofilin(wt), pcDNA3-EGFP-cofilin(S3D) and pcDNA3-EGFP-cofilin(S3A) (ref. 56); pEGFP-Par3(wt), pEGFP-Par3(T833D) and pEGFP-Par3(T833A) (ref. 57); pEGFP-Myosin-IIA and pEGFP-Myosin-IIAN93K27 (ref. 10); Addgene plasmids: 13719 pcDNA3-EGFP-Rac1(wt), 13720 pcDNA3-EGFP-Rac1(Q61L) and 13721 pcDNA3-EGFP-Rac1(T17N; ref. 58); 12599 pcDNA3-EGFP-Cdc42(wt), 12600 pcDNA3-EGFP-Cdc42(Q61L) and 12601 pcDNA3-EGFP-Cdc42(T17N) (ref. 59); 12965 pcDNA3-EGFP-RhoA-wt, 12968 pcDNA3-EGFP-RhoA-Q63L and 12967 pcDNA3-EGFP-RhoA-T19N (ref. 60); 20671 pHJ320/EGFP-Moesin-wt, 20677 pHJ322/EGFP-Moesin-T558D and 20676 pHJ321/EGFP-Moesin-T558A (ref. 61); and 35680 pEGFP-MRLC1-wt, 35682 pEGFP-MRLC1-T18D, S19D, and 35681 pEGFP-MRLC-T18A, S19A (ref. 62). Fluorescent protein expression vectors containing the Lifeact sequence were constructed using N1 (Clontech) cloning vectors where EGFP was replaced with mEmerald (wtGFP with the following mutations: F64L, S65T, S72A, N149K, M153T, I167T and A206K) or mCherry. To insert the Lifeact sequence, the appropriate N1 cloning vector was digested with NheI and BamHI followed by gel purification. cDNA encoding the Lifeact sequence was obtained from IDT: Aaact forward: 5'-CTAGCCGCCACCATGGGCGTGGCCGACTTGATCAAGAAGTTCGAGTCC ATCTCCAAGGAGGAGGGG-3' Lifeact reverse: 5'-GATCCCCCTCCTCCTGG AGATGGACTCGAACTTCTTGATCAAGTCGGCCACGCCCATGGTGG CG-3'. The complementary Lifeact cDNA sequences were annealed in TE buffer at a concentration of 50 μM and ligated directly into the NheI-BamHI-digested cloning vectors to produce fusions of Lifeact-mEmerald and Lifeact-mCherry.

To knockdown genes encoding major isoforms of non-muscle myosin II heavy chains in rat epithelial cells, IAR-2, cells were transfected with non-targeting siRNA (control) or validated ON-TARGETplus SMARTpool siRNA reagents (Dharmacon) targeting rat-specific *Myh9* (myosin IIA isoform) mRNA (cat. no. L-095070-02-0005) or rat-specific *Myh10* (myosin IIB isoform) mRNA (cat. no. L-098035-02-0005). Cells were analysed 72 h post-transfection using standard western blot or immunofluorescent analysis protocols. On the basis of quantitative densitometry of proteins, myosin IIA and myosin IIB knockdown efficiency was estimated as 84.7 ± 2.5% and 93.7 ± 1.2% respectively (3 repeats).

Drug treatments. The following pharmacological inhibitors were used: 25 μM myosin II inhibitor blebbistatin (Toronto Research Chemicals), 10 μM ROCK inhibitor Y-27632 (EMD), 1 μg ml⁻¹ Rho inhibitor I (cell permeable C3 transferase from *Clostridium botulinum*) (Cytoskeleton), 50 μM Cdc42 inhibitor ML 141 (Tocris Bioscience), 50 μM Rac1 inhibitor NSC 23766 (Tocris Bioscience), 0.5 μg ml⁻¹ microtubule-depolymerizing drug colcemid (Sigma-Aldrich), 0.5 μM actin-stabilizing toxin jasplakinolide (Sigma-Aldrich), 5 μM actin-disrupting drug latrunculin B (Calbiochem) in combination with 8 μM jasplakinolide (a part of the JLY mixture²¹), 25 μM Arp2/3 inhibitors and nonspecific compounds CK-666, CK-869, and CK-689, CK-312 (Calbiochem), 35 μM formin FH2 domain inhibitor SMIFH2 (Calbiochem), 5 μg ml⁻¹ vesicular transport inhibitor brefeldin A (Sigma-Aldrich), 0.5 μM pan-class I PI(3)K inhibitor BKM120 (Cellagen Technology), 10 μM PTEN inhibitor SF1670 (Cellagen Technology), and 25 μg ml⁻¹ phosphopeptide activator of PI(3)K, PDGFR²⁰-Y-P (Tocris Bioscience). Growth medium was supplemented with 1% DMSO (vol/vol) (Sigma-Aldrich) in control experiments.

Antibodies and immunofluorescence microscopy. The following antibodies were used: anti-myc tag antibody (clone 4A6), Alexa Fluor 488 conjugate, no. 16-224 (Millipore), anti-β-actin antibody (clone EP1123Y) no. 04-1116 (Millipore), anti-myosin II regulatory light chain 2/MRLC antibody no. 3674 (Cell Signaling Technology), anti-Arp2 component of the Arp2/3 protein complex antibody no. ab47654 (Abcam), anti-non-muscle myosin heavy chain IIA no. ab55456 (Abcam), anti-non-muscle myosin heavy chain IIB no. PRB-445P (Covance), anti-Golgi marker GM130 antibody no. 558712 (BD Pharmingen), and anti-GAPDH antibody no. ab9483 (Abcam). Directed against the species of primary antibodies, Alexa Fluor 488- and Alexa Fluor 568-conjugated IgG antibodies (Molecular Probes) were used as secondary antibodies. IRDye and VRDye secondary antibodies (LI-COR) were used for western blotting. Primary and secondary antibodies for immunofluorescence microscopy were used in 1:100 and 1:300 dilutions, respectively. Primary and secondary antibodies for western blotting were used in 1:1,000 and 1:3,000 dilutions, respectively. F-actin was visualized using Alexa Fluor 488- or Alexa Fluor 568-conjugated phalloidin (Molecular Probes). Cells were rinsed with warm (37 °C) PBS, fixed in 3% PFA/PBS for 15 min at 37 °C, permeabilized with 0.5% Triton X-100 for 5 min, and blocked with 3% BSA/PBS for 30 min at room temperature. Primary and secondary antibodies were diluted using 3% BSA/PBS. Incubation with antibodies, washing and mounting steps were performed according to standard protocols. Samples were imaged using a Yokogawa spinning-disc confocal system on a Nikon Ti inverted microscope equipped with a ×100 Plan Apo NA 1.4 objective lens. Optical sections along the Z axis were collected with a step size of 0.2 μm, using the Nikon Ti internal focus motor. Z-series were displayed as maximum Z-projections.

Western blotting. Cells were collected and resuspended in Laemmli buffer. Proteins were separated using sodium dodecyl sulphate polyacrylamide gel electrophoresis (SDS-PAGE) and transferred onto PVDF membranes. After incubation with primary and secondary antibodies, the membranes were visualized using the Odyssey CLx Infrared Imaging System (LI-COR). To estimate protein levels and compare them between different samples, protein bands were quantified by densitometric scanning using ImageJ software (NIH, <http://rsb.info.nih.gov/ij/index.html>). Multiple dilutions of cell extract were analysed to ensure that the western signal was linear within the analysed range for each protein probed.

G-actin incorporation *in situ* for the localization of barbed ends of actin filaments. To localize and quantify the relative number of polymerization-competent free barbed ends of actin filaments, live cells treated with 25 μM BBS at different time points were briefly permeabilized with 0.25 mg ml⁻¹ saponin in the presence of 0.5 μM actin purified from rabbit skeletal muscle and conjugated with an activated ester of rhodamine (Cytoskeleton). After the incorporation of extracellular rhodamine-actin into the intracellular F-actin network, cells were fixed and stained with fluorescein-phalloidin to visualize total actin polymer as previously described¹⁹. The incorporation of newly polymerized actin was then assayed using rhodamine/fluorescein ratio imaging.

Measuring levels of cytoplasmic G-actin. To assess the levels of G-actin in the cytoplasm, the DNase I/phalloidin staining method was used^{17,18}. Briefly, cells treated with 25 μM BBS at different time points were fixed in 4% formaldehyde (EM grade) with 0.32 M sucrose in the cytoskeleton buffer (10 mM MES, 138 mM KCl, 3 mM MgCl₂, 4 mM EDTA, pH 6.1) for 10 min at 37 °C. After permeabilization followed by blocking with 3% BSA/PBS, the samples were incubated with 0.3 μM Alexa Fluor 488-DNaseI and 1:2,000 Alexa Fluor 568-conjugated phalloidin (Molecular Probes). Confocal Z-stacks on subtraction of the background fluorescence were used to measure total integrated fluorescence of DNaseI and phalloidin in individual cells. To avoid changes in G-actin levels associated with cell size heterogeneity, DNaseI and phalloidin fluorescence levels were normalized for cell size. In our experiments, an increase in G-actin levels (DNaseI fluorescence) was always associated with a decrease in F-actin levels (phalloidin fluorescence).

Live-cell imaging. Cells were plated on glass-bottomed 35-mm dishes (Fluoridishes). Phenol red-free DMEM/F-12 medium supplemented with 10% FBS (Invitrogen), 10 mM lactate, and OxyFluor (Oxyrase) was used during image acquisition, with a layer of mineral oil on top of the medium to prevent evaporation. Time-lapse series were collected with a Yokogawa spinning-disc confocal system on a Nikon Ti inverted microscope equipped with a 37 °C, 5% CO₂ incubation chamber, a ×100 Plan Apo NA 1.4 objective lens, solid-state lasers for 491 nm (100 mW) and 561 nm (200 mW) excitation, and the Perfect Focus System for continuous maintenance of focus. Images were acquired with a Hamamatsu ORCA-AG cooled CCD (charge-coupled device) camera controlled by MetaMorph 7.7 software (Molecular Devices). Image acquisition details are specified in the figure legends.

Cortical laser ablation (COLA). Cells were grown on No. 1.5 coverslips and mounted in a 20/20 Technologies Bionomic microscope stage heated chamber warmed to 37 °C. Phenol red-free DMEM/F-12 medium supplemented with 25 mM Hepes (pH 7.2), 10% FBS (Invitrogen), 10 mM lactate, and OxyFluor (Oxyrase) was used during image acquisition, with a layer of mineral oil on top of the media to prevent evaporation. Images were collected on a Nikon Ti-E inverted microscope equipped with a $\times 100$ Plan Apo NA 1.4 objective lens and a Prior Proscan II motorized stage. The Nikon Perfect Focus System was engaged to maintain a continuous plane of focus. An EXFO X-cite XL-120 epi-fluorescence light source was used for illumination of mEmerald, which was excited with a 480/40 excitation filter and collected with a 505 nm dichroic mirror and 535/50 emission filter from Chroma. For laser ablation experiments, an N2 pulsed dye-tunable Micropoint System tuned to 553 nm with MetaMorph controlled galvos for beam positioning was used (Photonic Instruments). Live-cell time-lapse data series were acquired using a Hamamatsu ORCA R2 cooled CCD camera controlled by MetaMorph 7.7 software.

Microfabricated tools for restricting cell motility and controlling cell shape. Microfabricated substrates of different configurations (microchannels with nanofabricated walls or circular/linear stamps of fibronectin interspaced by non-adhesive areas) were obtained from CYTOO.

3D Matrigel cell culture. MCF-10A cells (ATCC) were validated by STR profiling at ATCC and cultured as described previously (<http://brugge.med.harvard.edu/protocols>). Wells of an 8-well glass chamber slide (Becton Dickinson) were coated with Matrigel (BD Biosciences). Five thousand cells were counted and mixed with cold Matrigel. The mixture was overlaid on top of Matrigel contained within each well of the glass chamber slide, allowed to solidify at 37 °C, and standard growth medium was then added to the cells. After 24–48 h, 3D cultures were fixed with 3.7% PFA/PBS, blocked and stained with 5% BSA, 5% FBS, 5 $\mu\text{g ml}^{-1}$ DAPI and 5 U ml^{-1} Alexa Fluor 488–phalloidin. Confocal Z-series were acquired with a 1- μm step size, using a Nikon C1si point scanning confocal microscope equipped with a Plan Fluor multi-immersion 20 \times 0.75 NA lens. MetaMorph 7.7 software was used for 3D reconstruction of the acquired stacks.

Quantitative image analysis. For COLA measurements, positions of laser-ablated ends of F-actin structure were tracked from a kymograph of a COLA time-lapse video. The kymographs were constructed using a custom code in Matlab 8.1 software (MathWorks). Edge velocity was calculated by the slopes of regression lines of 3 consecutive data points in time–position data.

ImageJ software (NIH, <http://rsb.info.nih.gov/ij/index.html>) was used to acquire binary images of F-actin-stained cells and automatically trace cell outlines for measurements of cell surface area (A) and perimeter (P). Circularity ($4\pi(A/P^2)$) was calculated as a normalized ratio of A to P , with a value of 1 representing a perfect circle and a value close to 0 representing more elliptical or elongated surfaces. Aspect ratio (AR) was calculated as a ratio of major cell axis length to minor cell axis length, automatically determined by ImageJ software. An AR value of 1 corresponds to a highly symmetric object.

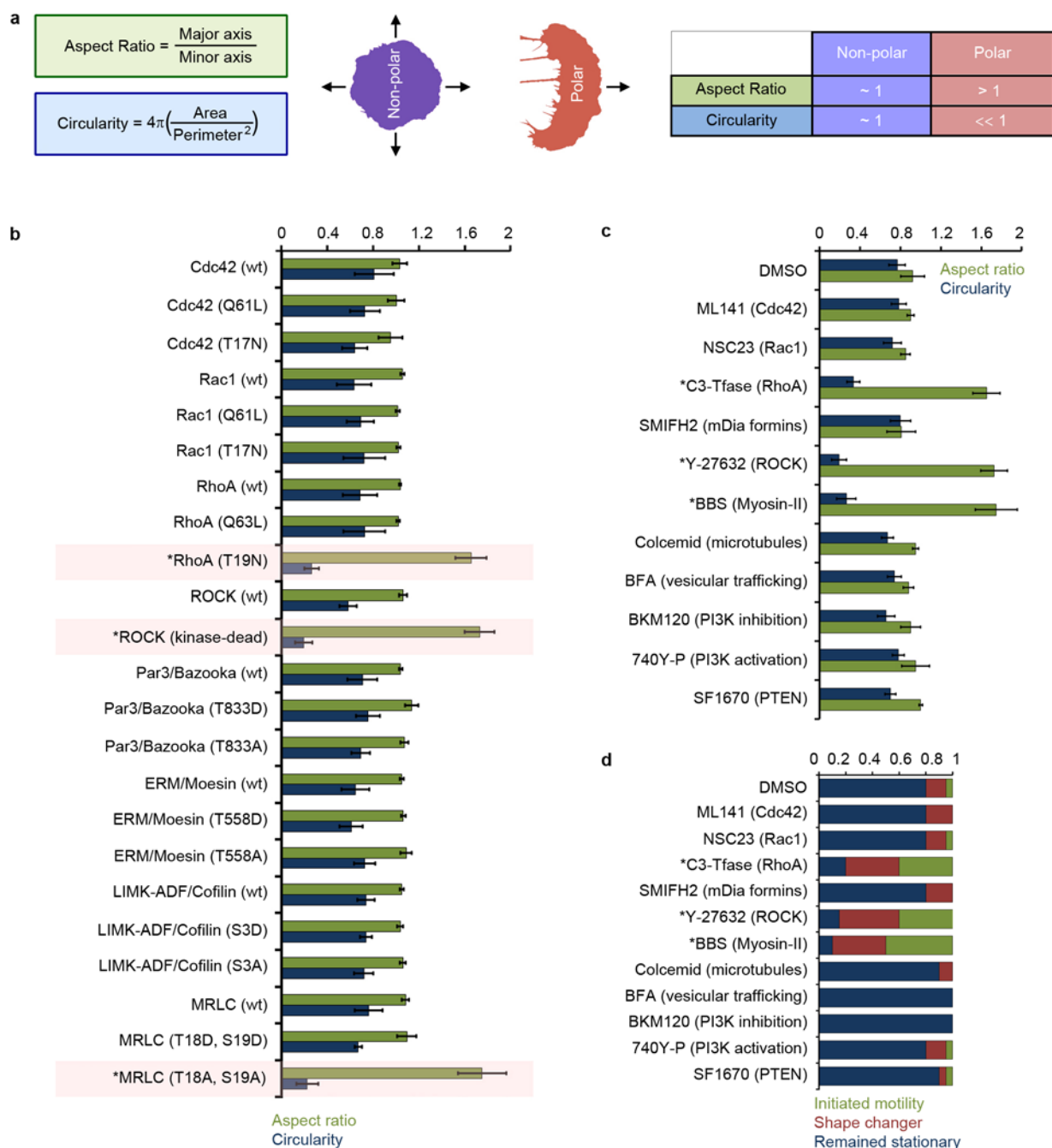
Protrusivity was defined as a distance of a cell edge from an average protrusion–retraction cycle. Edge velocities and persistence time at each protrusion/retraction phase of live mEmerald–LifeAct-expressing cells were determined using a custom-written software package⁶³. The obtained parameters were averaged. The mean velocities and persistence time were used to calculate the average edge displacement (d_p) as $d_p = v_p t_p - v_r t_r$, where v_p is the protrusion velocity, t_p is the protrusion persistence time, v_r is the retraction velocity, and t_r is the retraction persistence time.

MRLC patches were tracked using time-integrated cross-correlation tracking⁶⁴ with 3 frames of the time window for evidence accumulation and templates of 11×11 pixels (1 pixel = 72 nm). Grid points with 3-pixel spacing were used to track motions of myosin II. The tracking was validated using standard kymographic analysis; results obtained with these two methods were highly consistent. Centripetal flow of actin bundles was analysed using the Kymograph function in MetaMorph 7.7 software. Manual kymographic analysis or automated quantitative fluorescent speckle microscopy⁶⁵ tools were applied to analyse the retrograde actin flow in lamellipodial regions of cells expressing low levels of Lifeact. The actin polymerization rate was calculated as the sum of the retrograde actin flow and the forward protrusion at the leading edge. To quantitatively characterize the degree of coupling between actin and myosin flows in the same cell, the technique of correlational fluorescent speckle microscopy³² was employed. The direction coupling score was measured by $\cos\theta$ (θ : the angle between myosin II and F-actin displacement vectors within a pair). A score of 1 defines two vectors with identical directionality and a score of -1 defines two vectors that point in opposite directions. The velocity magnitude coupling score (VMCS) is the ratio between the magnitude of the coupled components of F-actin and myosin II speckle motions, minimizing the influence of random fluctuations. A detailed description of VMCS is provided in ref. 32.

Statistics and reproducibility of experiments. Unless stated otherwise, statistical significance was determined by two-tailed unpaired Student's t -test after confirming that the data met appropriate assumptions (normality, homogeneous variance and independent sampling). Statistical data are presented as average \pm either s.e.m. or s.d. Sample size (n) and P value are specified in the text of the paper or figure legends. Samples in most cases were defined as the number of cells counted/examined within multiple different fields of view on the same dish/slide, and thus represent data from a single sample within a single experiment, that are representative of at least three additional independently conducted experiments.

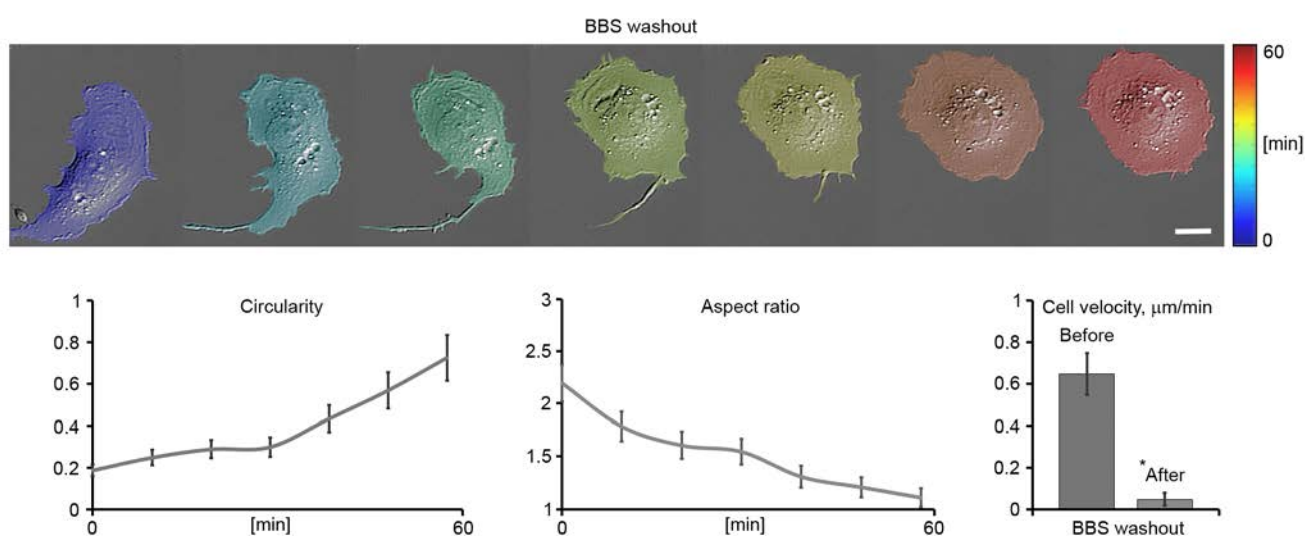
55. Ishizaki, T. *et al.* p160ROCK, a Rho-associated coiled-coil forming protein kinase, works downstream of Rho and induces focal adhesions. *FEBS Lett.* **404**, 118–124 (1997).
56. Pontrello, C. G. *et al.* Cofilin under control of β -arrestin-2 in NMDA-dependent dendritic spine plasticity, long-term depression (LTD), and learning. *Proc. Natl Acad. Sci. USA* **109**, E442–E451 (2012).
57. Nakayama, M. *et al.* Rho-kinase phosphorylates PAR-3 and disrupts PAR complex formation. *Dev. Cell* **14**, 205–215 (2008).
58. Kraynov, V. S. *et al.* Localized Rac activation dynamics visualized in living cells. *Science* **290**, 333–337 (2000).
59. Nalbant, P., Hodgson, L., Kraynov, V., Touthckine, A. & Hahn, K. M. Activation of endogenous Cdc42 visualized in living cells. *Science* **305**, 1615–1619 (2004).
60. Subauste, M. C. *et al.* Rho family proteins modulate rapid apoptosis induced by cytotoxic T lymphocytes and Fas. *J. Biol. Chem.* **275**, 9725–9733 (2000).
61. Hao, J. J. *et al.* Phospholipase C-mediated hydrolysis of PIP2 releases ERM proteins from lymphocyte membrane. *J. Cell Biol.* **184**, 451–462 (2009).
62. Beach, J. R., Licate, L. S., Crish, J. F. & Egelhoff, T. T. Analysis of the role of Ser1/Ser2/Thr9 phosphorylation on myosin II assembly and function in live cells. *BMC Cell Biol.* **12**, 52 (2011).
63. Machacek, M. & Danuser, G. Morphodynamic profiling of protrusion phenotypes. *Biophys. J.* **90**, 1439–1452 (2006).
64. Ji, L. & Danuser, G. Tracking quasi-stationary flow of weak fluorescent signals by adaptive multi-frame correlation. *J. Microsc.* **220**, 150–167 (2005).
65. Mendoza, M. C., Besson, S. & Danuser, G. Quantitative fluorescent speckle microscopy (qFSM) to measure actin dynamics. *Curr. Protoc. Cytom.* **2** (2012).

DOI: 10.1038/ncb3246



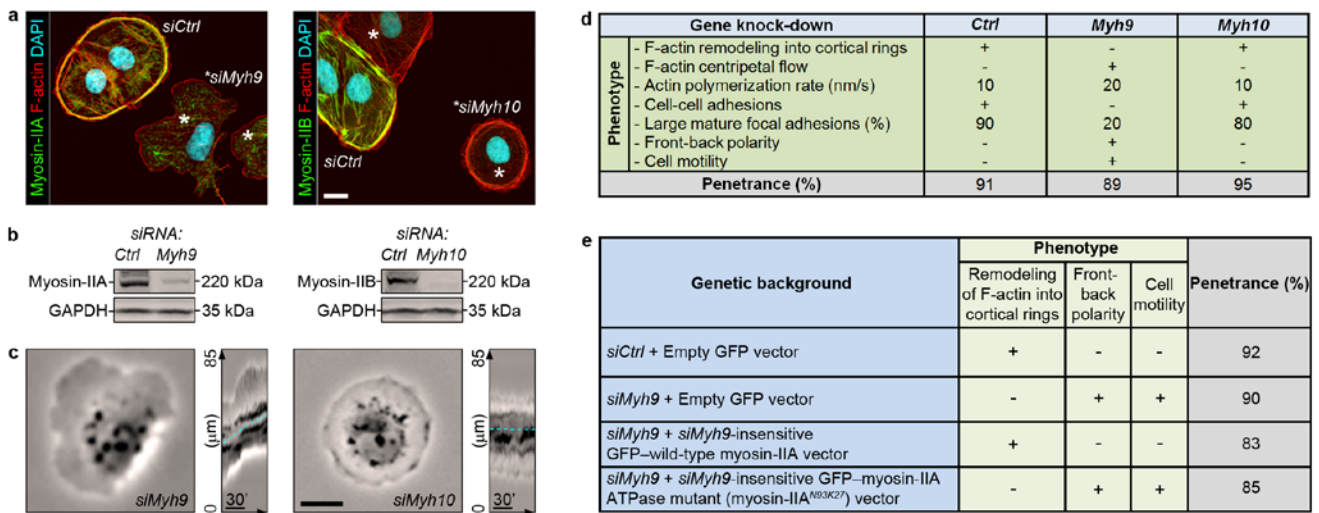
Supplementary Figure 1 Quantitative analyses of large-scale morphodynamics in cultured epithelial cells IAR-2 in different signaling states. **a**, Cell shape descriptors (circularity and aspect ratio) and representative “masks” of cells in a non-polarized and polarized state. **b**, Shape descriptors measured in cells over-expressing wild-type (wt), constitutively active mutant (Q61L/Q63L; “ON-state”), and dominant negative mutant (T17N/T19N; “OFF-state”) versions of Cdc42, Rac1, RhoA, and the key components of the ROCK signaling pathway carrying activating (D) or inactivating (A) phosphomutations in ROCK-specific phosphorylation sites (n = 80 cells per each experimental condition; Mean ± SEM; *p < 0.001, two-tailed unpaired Student’s t-test). **c**, Modulation of RhoA-regulated formin-dependent actin polymerization, the microtubule cytoskeleton, vesicular trafficking, and chemotactic phosphoinositide signaling

reactions *per se* is insufficient to induce migratory cell polarization in stationary epithelial cells. However, inhibiting RhoA/ROCK-dependent myosin-II activity alone produces cells with a polarized phenotype. Shape descriptors measured after 5 hours of incubation with various small-molecule inhibitors (n = 120 cells per each experimental condition; Mean ± SEM; *p < 0.001, two-tailed unpaired Student’s t-test). Targets of the inhibitors are specified in parentheses. **d**, Proportion of cells remaining stationary, changing shape, or initiating motility within 4 hours after addition of various inhibitors. Motility initiation was defined as an asymmetric, front-rear morphology and cell body displacement persisted over at least three cell lengths. Shape changers were non-polarized cells frequently switching between irregular shapes (n = 50 cells per each experimental condition; *p < 0.001, two-tailed unpaired Student’s t-test).



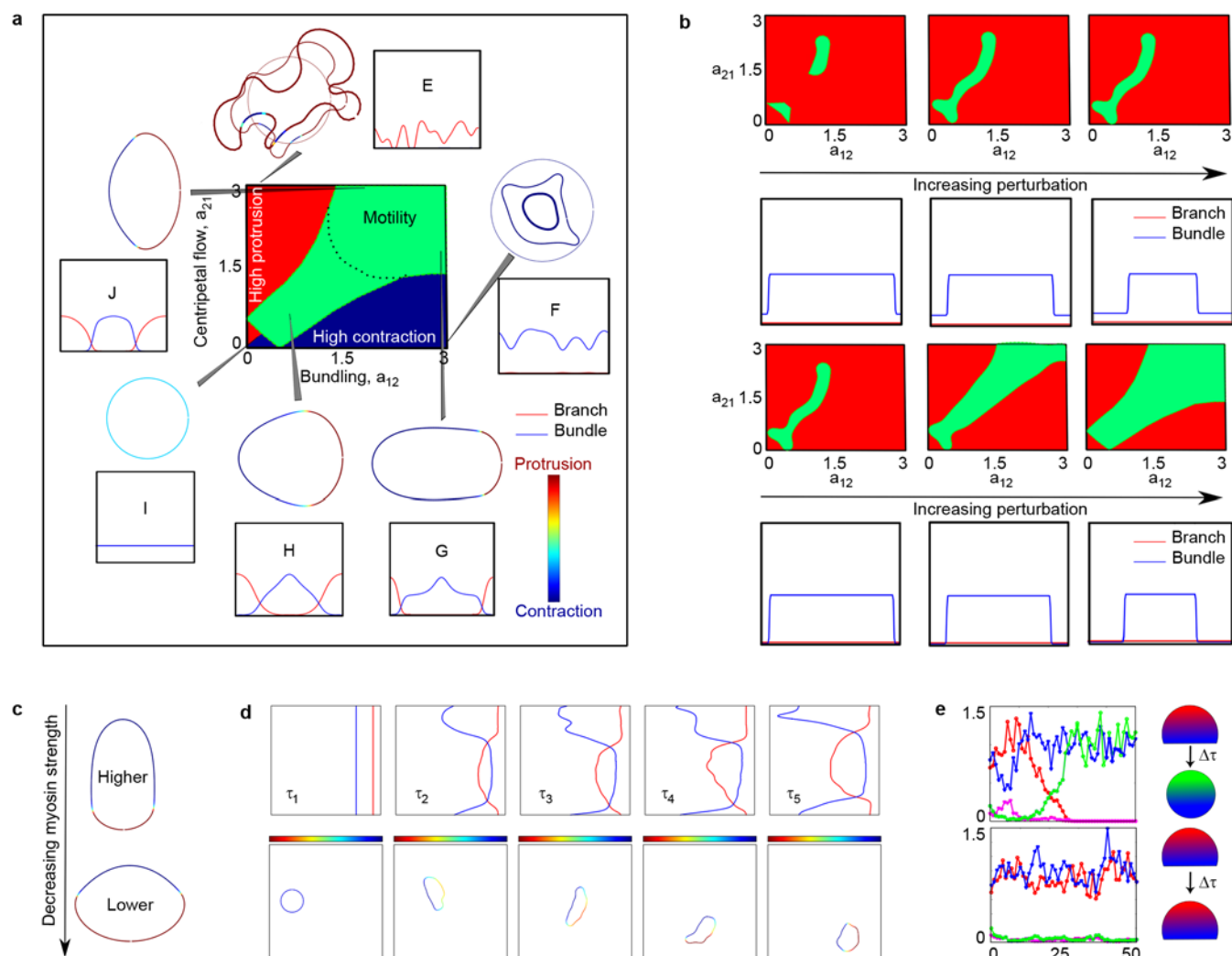
Supplementary Figure 2 Increasing myosin-II activity switches migratory polarized epithelial cells back to stationary unpolarized morphologies. Low levels of myosin-II activity in epithelial cells treated with 25 μM blebbistatin (BBS) are associated with spontaneous polarization and migration (Fig. 1). To increase myosin-II activity in such cells, BBS washout experiments were performed. The representative video sequence

shows cells immediately after BBS washout. Scale bar, 10 μm . Removing BBS from the culture medium and thus increasing myosin-II activity restores typical stationary organization of epithelial cells, which is reflected in increased circularity, decreased aspect ratio and cell velocity ($n = 30$ cells, Mean \pm SD – applies to all 3 graphs; $*p < 0.001$, paired samples t-test).



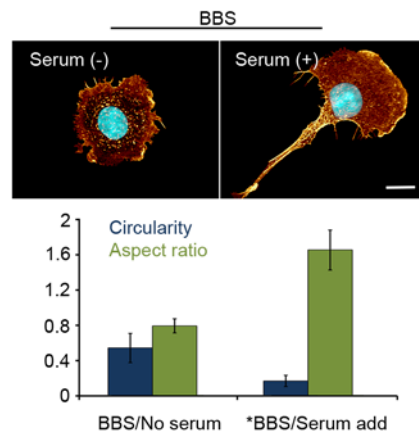
Supplementary Figure 3 Isoform-specific effect of myosin-II on migratory cell polarity in epithelial cells. **a**, IAR-2 cells were transfected separately with nontargeting siRNA (Control), siRNA targeting *Myh9* mRNA that encodes myosin-II A isoform, and siRNA targeting *Myh10* mRNA that encodes myosin-II B isoform. After transfection, two types of cell mixtures (1:1) were obtained: (1) *Myh9* siRNA + Control siRNA and (2) *Myh10* siRNA + Control siRNA. Correlation of cell morphology (F-actin staining, red) with endogenous protein levels (myosin-II A- and myosin-II B-isoform-specific antibody staining, green) was conducted 72 hr after transfection, as at this time minimal protein levels were detected. Unlike *Myh10* siRNA-transfected cells, *Myh9* siRNA-transfected epithelial cells lose actin rings, break cell-cell adhesions, and change shapes. Asterisk, *Myh9* or *Myh10* siRNA-transfected cells. Scale bar, 10 μ m. **b**, Western blotting-based evaluation of endogenous protein levels in cell lysates obtained 72 hr after transfection with siRNA

reagents. **c**, Phase-contrast micrographs of live *Myh9* or *Myh10* siRNA-transfected cells. Next to each micrograph is a kymograph showing whole cell dynamics over time. Scale bar, 10 μ m. **d**, Phenotypic characteristics of cells treated with different siRNA reagents (n = 40 cells (*Ctrl*), 50 cells (*Myh9*), and 47 cells (*Myh10*); $P_{(Ctrl\ vs.\ Myh9)} < 0.001$, $P_{(Ctrl\ vs.\ Myh10)} > 0.5$, $P_{(Myh9\ vs.\ Myh10)} < 0.001$, two-tailed unpaired Student's t-test). **e**, Phenotypic characteristics of cells expressing different plasmid constructs and simultaneously treated with control or *Myh9* siRNA reagents (n = 44 cells (*siCtrl* + Empty vector), 48 cells (*siMyh9* + Empty vector), 45 cells (*siMyh9* + wild-type [wt] myosin-IIA), and 48 cells (*siMyh9* + myosin-IIA^{N93K27}); $P_{(siCtrl\ +\ Empty\ vector\ vs.\ siMyh9\ +\ Empty\ vector)} < 0.001$, $P_{(siMyh9\ +\ Empty\ vector\ vs.\ siMyh9\ +\ wt\ myosin-IIA)} < 0.001$, $P_{(siMyh9\ +\ wt\ myosin-IIA\ vs.\ siMyh9\ +\ myosin-IIA^{N93K27})} < 0.001$, two-tailed unpaired Student's t-test. Only cells expressing levels of exogenous protein comparable to that of endogenous protein were used for the analyses.



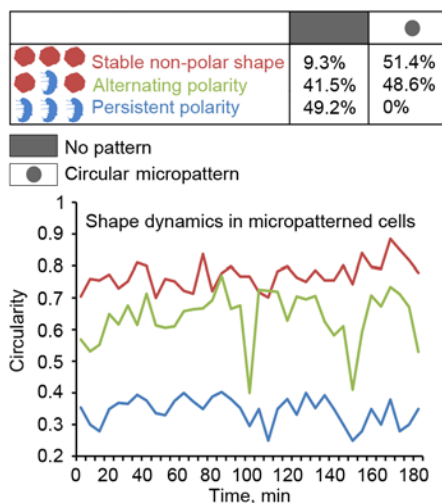
Supplementary Figure 4 Mathematical model predictions. **a**, Motility phase diagram and predicted cell shapes with actin network densities (blue, bundled actin; red, branched actin) below each shape. Thinner contours, earlier time points; thicker contours, later time points in stochastic simulations for Cell E (very high protrusion strength: $a_{12} = 0.1$, $a_{21} > 3$) and F (very high myosin strength: $a_{12} > 3.0$, $a_{21} = 0.1$). **b**, Dependence of the phase diagram on initial perturbations. Each simulation begins with a high bundled actin density everywhere. After some equilibration time (10 time units), a segment of bundled actin is ablated locally. The resulting bundled actin densities (blue) are step-function-like, with a sharp drop in the ablated area. The branched actin densities (red) are set to a low constant value. The width of the ablated bundled actin increases from left to right (left = 10%, middle = 20%, right = 50%). Top row, cases in which the drop in the bundled actin density is 80% of the initial value. Bottom row, cases in which the drop in the bundled actin density is 100% of the initial value. **c**, Cell shape changes with

increasing myosin inhibition. **d**, Simulation of cells with stochastic F-actin dynamics. $\tau_1 < \tau_2 < \tau_3 < \tau_4 < \tau_5$, simulation time points. **e**, 1D model with the global slow feedback. Top, simulation of the stochastic model without the feedback. The cell initially polarizes by establishing asymmetries in the density of branched vs. bundled actin along the front-back axis. However, with time, stochastic fluctuations in myosin/actin densities can depolarize the cell. A representative case where bundled actin spontaneously "wins" at the front is shown. Bottom, simulation of the stochastic model with the global feedback from long-range actin-myosin transport. The cell polarizes and is able to maintain its polarity because rearward actin-myosin transport and forward cell motion keep myosin density biased, dampening the stochastic fluctuation effect at the back. Red, branched actin at the front; Blue, bundled actin at the back; Magenta, branched actin at the back; Green, bundled actin at the front. X-axis, time; Y-axis, actin density (a.u.). Cartoon next to the graphs, a 2D interpretation of the simulations.



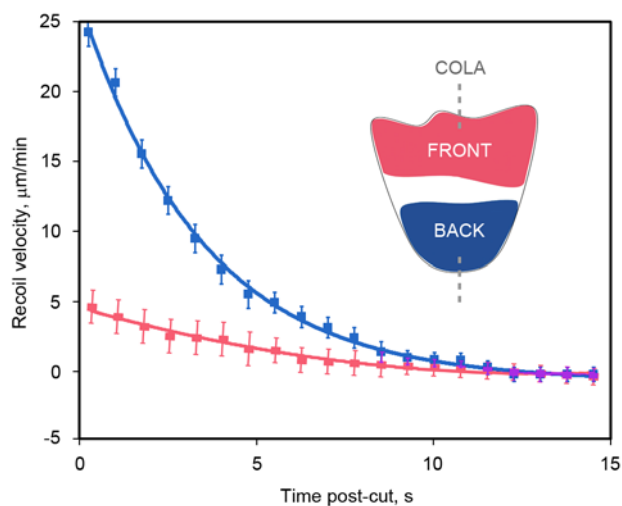
Supplementary Figure 5 Presence of serum in the growth medium is required for migratory cell polarization upon partial inactivation of myosin-II with blebbistatin. IAR-2 cells were kept in fetal bovine serum (FBS)-free growth media for 5 hours; after this step, the growth medium was changed and cells were cultivated for 3 hours in the media containing 25 μM blebbistatin

and 10% FBS (Serum add), or 25 μM blebbistatin and no FBS (No serum). By the end of the experiment, cells were fixed and stained for F-actin and nuclear DNA, and cell shape descriptors were statistically evaluated per each experimental condition ($n = 80$ cells for each case, Mean \pm SEM; $*p < 0.001$, two-tailed unpaired Student's t-test). Scale bar, 10 μm .



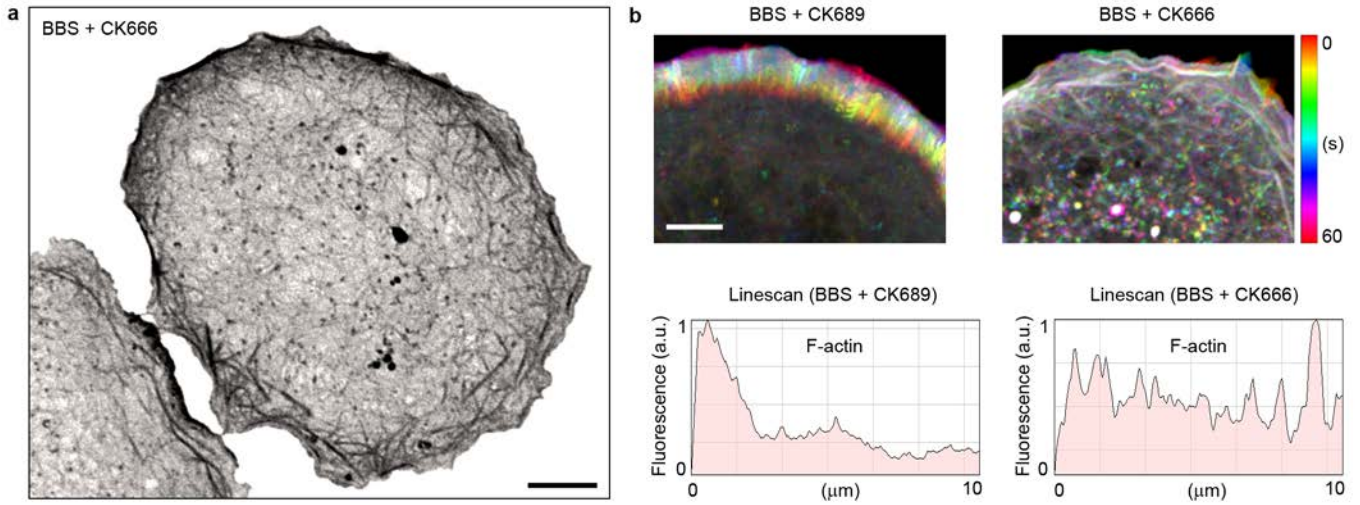
Supplementary Figure 6 Motility-arrested cells fail to stabilize front-back asymmetry emerging upon myosin-II suppression. The table displays percentage of cells with a specific morphodynamic behavior observed on substrates with uniform fibronectin coating ($n = 45$ cells) or on the microfabricated fibronectin pattern ($n = 50$ cells; $p < 0.001$, two-tailed unpaired Student's t -test). The graph in which cell shape circularity index is

plotted over time shows that BBS-treated cells on unpatterned fibronectin establish robust steady-state front-back asymmetry (low circularity, blue). In contrast, BBS-treated cells on circular fibronectin patterns rest in an unpolarized state (high circularity, red) or exhibit short bursts of frustrated front-back asymmetry that immediately return to an unpolarized state because of the missing ability to move forward (high circularity, green).



Supplementary Figure 7 Spatial differences in F-actin contractility exposed by localized cortical laser ablation (COLA) of the actin cytoskeleton in a polarized epithelial cell. A two micron-sized laser cut was made at the branched actin-rich front and bundled actin-containing back pole of IAR-2 epithelial cells expressing mCherry-LifeAct and pretreated with BBS for 5 hours ($n = 10$ cells; Mean \pm SEM). The degree of local F-actin contractility at the front vs. back of the cell was

estimated from the initial recoil velocity of F-actin material adjacent to the laser cut. Assuming that contractility is a function of density of mechanochemically-active myosin-II motors and that the coefficient of friction is the same for actin filaments at the front and back poles of the cell, the analysis reveals a functional asymmetry of distinct cell poles in a migratory polarized cell: unlike the front, the back end of the cell displays contractile properties.



Supplementary Figure 8 Spatiotemporal organization of F-actin in Arp2/3-inhibited epithelial cells at low contractility regimes. **a**, F-actin organization in a myosin-inhibited cell with suppressed Arp2/3 activity (BBS + CK666). Scale bar, 5 μm . **b**, F-actin dynamics in myosin-inhibited cells with functional Arp2/3 (BBS + CK689) and suppressed Arp2/3 activity (BBS + CK666).

Zoomed fragments of cells are shown. F-actin (labeled with mCherry-LifeAct) was imaged with a 5-second interval for 60 seconds. Each timeframe from the movie was color-coded and the entire movie presented as a maximum projection of all timeframes. Color scale, time in seconds. Linescans, F-actin fluorescence intensity from the cell edge to the cell center. Scale bar, 1 μm .

Supplementary Videos

Supplementary Video 1 A single IAR-2 epithelial cell 24 hours after plating on a glass surface. Differential interference contrast (DIC) videomicroscopy. Time, hours:minutes. Scale bar, 10 μm .

Supplementary Video 2 Spontaneous symmetry breaking upon acute inhibition of myosin-II. DIC movie is shown on the left; tracking of the cell boundary based on the time sequence of DIC images is shown on the right. IAR-2 cells were pretreated with 25 μM blebbistatin for ~5 minutes and subsequently imaged in blebbistatin-containing medium. Time, hours:minutes. Scale bar, 10 μm .

Supplementary Video 3 A myosin-II-inhibited epithelial cell IAR-2 ~3 hours after addition of the myosin-II drug blebbistatin. DIC videomicroscopy. Time, hours:minutes. Scale bar, 10 μm .

Supplementary Video 4 The recoil response of a marginal actin bundle upon localized cortical laser ablation (COLA). A peripheral region of an IAR-2 cell expressing mEmerald-LifeAct and filmed by spinning disk confocal microscopy. The site of ablation is marked by a square; white arrows show the free ends of the ring upon ablation. Time, minutes:seconds. Scale bar, 3 μm .

Supplementary Video 5 Mass-balance between branched and bundled actin in cell shape and polarity determination (1). At myosin strengths lower than in control situations, the bundled actomyosin and branched actin networks spatially segregate around the cell boundary while the cell polarizes, and stable cell motility ensues. The dynamic cell boundary is shown in the coordinate system moving with the geometric center of the cell; hence, the cell appears stationary, while in fact it is moving steadily to the right, which is shown below and also by the grid moving with the lab frame. Color scale, red – protrusion; blue – retraction.

Supplementary Video 6 Mass-balance between branched and bundled actin in cell shape and polarity determination (2). In a control situation, the bundled actomyosin network effectively inhibits the branched actin networks all around the cell periphery. The cell remains symmetric and non-motile. Initial perturbations relax and do not destabilize the symmetric cell state. An intense perturbation is introduced closer to the end of the movie that wipes out part of the actomyosin bundle. The cell becomes motile temporarily and quickly reverts into the stationary symmetric circular state. Color scale, red – protrusion; blue – retraction.

Supplementary Video 7 Mass-balance between branched and bundled actin in cell shape and polarity determination (3). At very low myosin strength, the branched actin network effectively inhibits the bundled actomyosin all around the periphery causing incoherent symmetry breaking of the cell but not coherent motility. Color scale, red – protrusion; blue – retraction.

Supplementary Video 8 Acute inhibition of myosin-II in stationary epithelial cells stimulates retrograde flow of myosin-II concomitant with the depletion of cortical myosin-II from the cell edge. IAR-2 cells expressing mCherry-MRLC were pretreated with 25 μM blebbistatin for ~5 minutes and subsequently imaged by spinning disk confocal microscopy in blebbistatin-containing medium. Time, minutes:seconds. Scale bar, 1 μm .

Mathematical Model

We used mathematical modeling to complement experimental methods with a tool that allowed us to vary essential mechanical and chemical parameters and then test whether the microscopic effects of myosin-based reorganization of the F-actin network would be sufficient to explain the large-scale shape changes and induction of epithelial cell motility we observed experimentally. In essence, the model describes the dynamic competition of two distinct actin network structures in a “winner-takes-all” modality: The first network structure is branched and devoid of myosin-II. Instead, it actively assembles to generate propulsive forces against the membrane. The second network contains contractile actomyosin bundles that tend to retract the cell edge. Relying on Turing’s classic model of morphogenesis¹, the first network can be considered as an activator, while the second as an inhibitor of migratory cell polarity. In this sense, Arp2/3-facilitated protrusion of the leading edge activates cell polarity at the front, whereas myosin-II-driven retraction of the trailing edge inhibits cell polarity at the cell rear.

In the following we discuss in detail the model equations describing the network dynamics, how the dynamics are linked to cell boundary movement, and the predictions that can be made from this mathematical treatment. Then, we discuss how the model equations can be derived from fundamental laws of mass conservation and force balance. The section continues with a discussion of the effects of initial conditions and stochastic perturbations on the model behavior. The section concludes with examining the additional feedback between activation of cell polarity at the front and its inhibition at the rear *via* the long-range actomyosin flows that emerge upon down-tuning of actomyosin contractility in epithelial cells.

Model equations

We consider the dynamics of the branched actin network, $A(\theta,t)$, and the bundled actin filaments, $B(\theta,t)$, along the cell boundary in polar coordinates along the cell edge with $0 < \theta < 2\pi$. The strength of myosin, M , determines the magnitude of the bundling term. $V(\theta)$ denotes the local cell edge velocity in polar coordinates and T denotes the membrane tension. The model consists of three equations:

$$\frac{\partial A}{\partial t} = \left(\frac{r_1 + k_1 V(\theta)}{4\lambda_2} \right) A - a_1 A^2 - q_{12} \left(\frac{M}{2} \right) \frac{AB}{\lambda_3} - d_1 AB + D_{12} \nabla^2 A \quad \nabla \quad \text{S.1a}$$

rate of change of branched actin growth of branched actin; enhanced with local protrusion and inhibited with local retraction growth is limited at high density by lack of molecular resources bundling term competition for G-actin term lateral flow

$$\frac{\partial B}{\partial t} = \left(\frac{r_2 - k_2 V(\theta)}{4\lambda_2} \right) B - a_2 B^2 + q_{12} \left(\frac{M}{2} \right) \frac{AB}{\lambda_3} - a_1 AB + D_{12} \nabla^2 B \quad \text{S.1b}$$

rate of change of bundled actin growth of bundled actin; enhanced with local retraction and inhibited with local protrusion growth is limited at high density by lack of molecular resources bundling term competition for G-actin, plus bundled actin is moved away from the cell edge by local centripetal flow myosin shuffling

$$V(\theta) = \frac{V_p A(\theta)^m}{1 + \frac{A(\theta)^m}{\lambda_1} + \frac{A(\theta)^m}{\lambda_2} + \frac{A(\theta)^m}{\lambda_3}} - \frac{V_r B(\theta)^m}{1 + \frac{B(\theta)^m}{\lambda_1} + \frac{B(\theta)^m}{\lambda_2} + \frac{B(\theta)^m}{\lambda_3}}, \quad T = T_0 \frac{Area^{s+1}}{Area^s + Area_0^s} \quad \text{S.1c}$$

local net radial extension local protrusion rate local retraction rate membrane tension

Densities of both actin networks are defined on the periodic cell boundary. The first terms in both Eq. S.1a and Eq. S.1b describe autocatalytic growth of the actin networks, *i.e.* the rate of growth is proportional to concentration. This autocatalytic growth is due to the assumption that at certain average actin filament length regulated by the elongation and capping rates, the filament (and their ends) number is proportional to the actin density. In the case of the bundled network then, we assume that the net growth rate is proportional to the number of the uncapped barbed ends, and in the case of the branching network to the number of existing filaments. In both cases, therefore, the net growth rates are proportional to the current local densities. By assuming a constant average filament length the densities can be measured either in unit of filament length, or in unit of filament number. The second terms in Eq. S.1a and Eq. S.1b describe the limits of actin network growth. In the case of the branched actin network, this term describes growth limits due to depletion of either G-actin or Arp2/3 complexes. In the case of the bundled actin network, this term describes growth limits due to depletion of the myosin-II or G-actin, or other factors that affect the bundling process of actin filaments.

In Eq. S.1a, the third term describes the decrease in branched F-actin density conversion into bundled filaments accompanied by a corresponding increase in bundled F-actin density in Eq. S.1b (third term). We assume the rate of this bundling process follows mass action, *i.e.* it is proportional to the product of the branched and bundled actin densities. Our experimental observations demonstrate that even without a significant forward displacement of the cell over its substrate, the bundled actin still moves centripetally inward. This movement is negligible in control, but when myosin is partially inhibited (Fig. 7a), the centripetal flow of the bundles is noticeable. Below, we analyze the mechanics of this flow and demonstrate that this effect gives rise to the fourth term in Eq. S.1b. Moreover, we demonstrate that the centripetal flow is described by mass action, *i.e.* as with the bundling itself, it is proportional to the product of the branched and bundled actin densities. The fourth terms in Eqs S.1a and S1b are responsible for the competition of both networks for the common G-actin pool. The derivation of these terms is exactly the same as that in the classical ‘competition for resources’ model of population dynamics²: if total local actin amount is equal to \bar{A} then local amount of G-actin is $(\bar{A} - A - B)$. Then,

the F-actin assembly rate for either network is proportional to the product of the G-actin concentration and barbed end density (which, in turn, is proportional to respective F-actin density), and thus the assembly rates for the branched and bundled networks are proportional to expressions $A(\bar{A} - A - B)$ and $B(\bar{A} - A - B)$, respectively. When the brackets in these expressions are open, terms $\bar{A}A$ and $\bar{A}B$ contribute to the first terms in Eqs S.1a and S1b, terms $-A^2$ and $-B^2$ to the second terms in Eqs S.1a and S1b, and terms $-AB$ to the competition for G-actin terms in Eqs S.1a and S1b. G-actin diffuses in the cytoplasm, and in principle this could make the model non-local, but realistically, as the actin turns over fast (estimates below), actin monomers diffuse but a couple of microns before assembling again³, justifying the local character of the respective terms. The last terms in Eqs S.1a and S1b describe the effective diffusive redistribution of the actin along the cell edge due to two processes: 1) as branched filaments grow, their barbed ends slide laterally along the cell edge (the phenomenon of lateral flow³); 2) myosin pulls and shuffles randomly bundled actin filaments along the edge⁴. It has been shown previously that Arp2/3-mediated F-actin meshworks compete for G-actin with formin- or Ena/VASP-assembled actin polymers to regulate size and structure of the bulk F-actin cytoskeleton⁵⁻⁷. Upon suppression of Arp2/3 activity, cells can assemble linear actin cables generated throughout the entire cell periphery by formins at the expense of the branched pool of actin normally focused at the leading edge of migrating cells^{8, 9}. This suggested that BBS + CK-666-treated cells in our experiments cannot polarize and initiate motility not because cells lost Arp2/3 activity *per se*, but because actin cable assembly starts dominating all around the cell periphery (Supplementary Fig. 8), precluding the formation of polarized lamellipodia. If formin-assembled actin networks and the formin-Arp2/3 competition on their own are significant for epithelial cell shape and polarity determination, up- or down-regulation of formin-mediated actin networks in epithelial cells with intact myosin activity should have an impact on the epithelial cell morphodynamics. Suppression of Arp2/3 with CK666 is expected to upregulate formin-mediated actin assembly, while formin inactivation with SMIFH2 should upregulate Arp2/3-dependent actin assembly. However, none of these perturbations had an effect on stationary epithelial cell morphology or motility initiation frequency (Supplementary Fig. 1c, d, and Fig. 4e). Accordingly, we did not consider in our model additional mechanisms of local competition between differentially nucleated actin networks structures.

A very important place in the model is allocated to the process of dynamic redistribution of branched and bundled actin populations that should be seen during the initiation of membrane protrusion (with the velocity $V(\theta)$) of myosin-inhibited cells. If the cell starts protruding in direction θ , then there is more branching in this direction because branched filaments grow and create nascent filaments from which new branches can appear (the phenomenon of autocatalytic growth of dendritic actin networks)^{10, 11}. Furthermore, at this location, the bundled actin is left behind the protruding edge. The latter substantiates a minimal step in local symmetry

breaking, as the dynamic separation between the two types of actin network leads to spatially graded conditions in which branched actin is favored at the prospective front and bundled actin is lagging behind and thus passively accumulating at the prospective rear. On the other hand, if there is a retraction of the cell boundary, the branching network gets crushed and absorbed into the bundles. Thus, if the local edge velocity $V(\theta)$ is negative, local branched actin would decrease and bundled actin would increase at rates proportional to the velocity and local densities. These processes couple the actin network dynamics to the local movements of the cell edge. Rigorous mathematical analysis¹² demonstrated that without the velocity feedback no stable, nontrivial spatial separation exists around the cell edge between two types of actin networks.

If the velocity is only a local function of the two network densities, simple simulations demonstrate that the local symmetry breaking event cannot get amplified to the degree of global cell shape polarization. This suggested that there should be some mechanism for long-range coupling between the local feedbacks. This follows also from Turing's theory¹³. Thus, as proposed by Houk *et al.*¹⁴, we hypothesize that membrane tension acts as the global coupler: when the cell area increases, tension increases and with it the growth of branched actin is slowed down. Hence, if branched actin concentrates at the front (as a result of stochastic fluctuations followed by the autocatalytic growth) and bundled actomyosin at the rear (due to the dynamic separation between the two networks), protrusion of the front and retraction of the rear are initiated and stabilized by the positive feedback provided by the membrane tension keeping the cell area constant and thus positive velocity at the front and negative at the rear, which in turn promotes the branched network at the front and the bundled network at the rear. To implement this feedback, we assume that the membrane tension is a simple function of the cell area (Eq. S.1c). It is very low if the area is smaller than a threshold at which the plasma membrane is completely floppy, and increases linearly with growing cell area above this threshold. The local rate of protrusion (first term in Eq. S.1c) increases as a function of the local branched actin density³ such that there is almost no protrusion if the branched actin density is below the threshold, $A_0(T)$, and saturates to a maximum if the density is very high. The threshold increases with the increasing membrane tension, which keeps the cell area constant on average. The net rate of cell boundary extension is the difference of the local protrusion and retraction rates. The retraction rate increased as a function of the local bundled actin density.

Mechanics and mass conservation laws and model parameters

In this sub-section, we justify the terms in the model equations and estimate model parameters. Equations S1.a-b are conservation laws for two actin networks, while Eq. S1.c is the constitutive law for the cell edge velocity that implicitly stems from the force-velocity relation for actin network growth. We will also use the balance of forces to justify expressions for some parameters in the model. The forces we will discuss include myosin

contractile force, membrane tension and effective friction from adhesion of the actin networks to the substrate. Specifically, small and dynamic nascent adhesions based on integrin molecules spanning the cell membrane interconnect the branched actin and the substrate. More mature focal adhesions, also integrin based but including many adaptors, force-sensing and signaling molecules, connect actomyosin bundles with themselves and the substrate. All these forces were extensively discussed in the literature¹⁵.

We note that the right-hand sides of equations S1.a-b rely on mass conservation, but the bundling and flow terms are implicitly based on force balances. Let us consider first the combination of terms

$$r_1 A - a_{11} A^2 = r_1 A \left(1 - \frac{a_{11}}{r_1} A \right)$$

in equation S1.a. Expression $r_1 \left(1 - \frac{a_{11}}{r_1} A \right)$ is the proportionality coefficient in the effective growth rate of the actin network. Parameter r_1 is the growth rate at low density unrestricted by limitations of molecular resources. It is of the same order of magnitude as the rate of F-actin turnover, which was previously measured by FRAP and other methods¹⁶, giving numbers of the order of inversed ten to hundred seconds. Our data gives the number closer to inversed ten seconds. We explored this whole range of rates; the results are not sensitive to the exact number (this is also clear from the non-dimensional analysis of the classical competition for resource model in population dynamics of two species². The expression in the brackets is the factor limiting the rate of growth as the F-actin density increases, similar to the fundamental logistic growth model. The simplest way to justify the functional form of this expression is to assume that the total local amount of actin (F- plus G-actin) is conserved, so the G-actin concentration is a linearly decreasing function of the F-actin concentration, and that the F-actin growth rate is proportional to the G-actin concentration (see above). Coefficient a_{11} has complex dependence on parameters of actin dynamics, but fortunately the details can be circumvented by observing that in equilibrium $\bar{A} = r_1 / a_{11}$ and using \bar{A} as the scale of F-actin density, and $1/r_1$ as the scale of time, we can re-write the first two terms in the non-dimensional equation S1.a in the form $(A - A^2)$. Similarly, the first two terms in the non-dimensional equation S1.b have the form $(r_2 / r_1)(B - B^2)$. Our data indicates that $r_2 \sim 0.01/\text{sec}$. For simplicity, in the simulations we use $r_1 = r_2 = 0.01/\text{sec}$ and so the first two terms in the non-dimensional equation S1.b have the form $(B - B^2)$ but the results hold if $r_1 > r_2$.

Thus, while parameters in the first two terms of equations S1.a-b are important, they just set the characteristic time scale for the model. To set the length scale, we use the observed characteristic rate of protrusion-retraction, $V_p = V_r \approx 0.01 \mu\text{m}/\text{sec}$ and define the length scale $V_p / r_1 = V_r / r_2 \approx 1 \mu\text{m}$. The simulations showed that several model parameters do not affect the qualitative behavior of the predictions. The effective diffusion coefficients

D_A and D_B , as long as they are small, do not affect the solutions. Coefficient D_A is easy to estimate: The branching process consists of a mother filament growing forward and sideways, and a daughter filament branching off and growing forward and to the other side. This is equivalent to making random steps to the right and to the left along the leading edge. The step duration is the characteristic time before capping, on the order of a few seconds¹⁷, and the step size is the protrusion over this duration, on the order of 0.1 microns. Accordingly, the respective diffusion coefficient is $(0.1\mu\text{m})^2/10\text{sec} \sim 0.001\mu\text{m}^2/\text{sec}$, which is an order of magnitude smaller than the length scale squared divided by the characteristic time, $(1\mu\text{m})^2/100\text{sec} \sim 0.01\mu\text{m}^2/\text{sec}$. Thus, the non-dimensional value for the diffusion coefficient that we use is $D_A = (0.001\mu\text{m}^2/\text{sec})/(0.01\mu\text{m}^2/\text{sec}) = 0.1$. For simplicity, we use the same non-dimensional value for D_B . Indeed, characteristic random displacements on the order of one tenth of a micron over a few to tens of seconds were observed in many motor gliding assays^{18, 19}.

Similarly, the exact values of parameters A_0 and B_0 and the function $A_0(T)$ do not qualitatively alter the results. In the simulations we use $A_0 = \pi(D/r_1) \sim 300 \mu\text{m}^2$. A few-fold variation of the dimensionless exponents s and m did not alter the character of the solutions, as long as $s > 2$ and $m > 2$: This reflects the fact that the local cell edge extension/retraction rate must have a sigmoidal, threshold-like dependence on the local actin density in order for the local cell edge to switch between protruding and retracting states. For the data presented, we used $s = 8$, $m = 4$. Note that equation S1.c is based on the force balance between the actin pushing force and membrane tension. We do not discuss this balance in detail because this analysis was done exhaustively in the literature; the sigmoidal, threshold-like dependence on the density was also established for the keratocyte lamellipodial actin network²⁰.

The term $(r_1 + k_1V(\theta))$ in equation S1.a describes the autocatalytic growth of branched actin during protrusion. We observed in our experiments with myosin-inhibited epithelial cells that in migratory polarized cells the density of branched actin at the leading edge increases about three-fold compared to the branched actin in unpolarized cell. Thus, $k_1V(\theta) \approx 2r_1$. We use the notation κ_1 for the non-dimensional parameter k_1V_p/r_1 . In simulations we used $\kappa_1 = 0.4$.

Term $(r_2 - k_2V(\theta))$ in equation S1.b describes the local rate of actin growth in the actomyosin bundle modified by the divergence of the bundle from the protruding leading edge. To estimate the coefficient k_2 , let us note that the effective divergence rate is equal to the local protrusion velocity divided by the characteristic length, which

accidentally corresponds to the width of the region where the flowing lamellipodial and filopodial actin interacts with the bundles. This rate is $\approx V_p / (V_p / r_1) = V_r / (V_r / r_2) = r_2$ and therefore the parameter k_2 is on the order of r_2 / V_r . $k_2 V_r$ has to be less than r_2 to make the expression $(r_2 - k_2 V(\theta))$ positive. We found that $k_2 V_r$ also has to be greater than a threshold ($\sim 0.3 r_2$) to sustain cell movement. For values smaller than this threshold, the cell does not polarize. This result highlights the importance of the coupling between cell movement and the feedback to actin dynamics for the polarization process. Once above the threshold value, the qualitative results do not change. We use the notation κ_2 for the non-dimensional parameter $k_2 V_r / r_2$. For this paper, our calculations used $\kappa_2 = 0.4$.

Two parameters in the model are of crucial importance: a_{12} , the bundling rate proportional to myosin strength, and a_{21} , the rate at which the local centripetal flow pushes bundles away from the edge. Let us consider the term $a_{12} AB = (a_{12} B) A$, where the expression in the bracket is the rate with which branched filaments are incorporated into the bundle. The mass-action form of this rate stems from the implicit assumptions of (1) the balance between the active bundling force pulling a branched filament into the bundle and the passive force of crosslinking and/or nascent adhesion keeping the branched filament as a part of the branched network, and of (2) proportionality of the active force to the bundled actin density. The latter is equivalent to the simplest assumption that the active force corresponds to the sum of myosin forces in which myosin, in order to pull, has to associate both with branched and bundled filaments. Thus, parameter a_{12} is proportional to the myosin strength. To estimate its order of magnitude, we note that the branched filaments in the unpolarized cell are all incorporated into the bundles on the time scale with which the lamellipodial and filopodial filaments flow centripetally from the leading edge to the bundle, $\approx 1 \mu\text{m} / (0.01 \mu\text{m} / \text{sec}) \approx 100 \text{sec}$. This is of the same order of magnitude as the actin turnover time scale $1 / r_1 \approx 100 \text{sec}$ and so the non-dimensional parameter $a_{12} \approx 1$.

Let us consider the term $a_{21} AB = (a_{21} A) B$, where the expression $a_{21} A$ is the rate of removal of the bundled actin by the flow. The proportionality of this rate to the branched actin density can be justified from the force balance between the membrane tension and strength of adhesions of the bundled actin to the substrate. Assuming viscous-like behavior of adhesions, the centripetal bundle flow rate $v \approx T / \zeta$ where ζ is the strength of the mature adhesions and T is the membrane tension²¹. The rate of the bundle removal is $\approx v / (1 \mu\text{m})$. The membrane tension is likely to be proportional to the density of branched filaments pushing on the membrane from within²², hence the proportionality of parameter $(a_{21} A)$ to A . To estimate parameter a_{21} , we relied on the observation that

in the cell treated with blebbistatin, remnants of actin bundles move centripetally with rate $\approx 0.01 \mu\text{m}/\text{sec}$ and so the rate of the bundle removal is $\approx 0.01 \mu\text{m}/\text{sec}/(1 \mu\text{m}) \approx 0.01/\text{sec}$. Thus, the non-dimensional value of parameter a_{21} is in the order of unity.

Finally, note that besides the mechanical processes leading to the bundling and flow term, there is a kinetic factor contributing to terms $a_{12}AB$ and $a_{21}AB$: the competition of the branched and bundled actin for the same G-actin pool (see above). Indeed, the terms $a_{11}A^2$ and $a_{22}B^2$ could be due to the fact that the G-actin concentration is depleted by F-actin growth. Hence, the G-actin concentration should be $G \propto F - c_1A - c_2B$ where F is the total actin concentration and $c_{1,2}$ are kinetic coefficients. Provided that the growth rates are proportional to G-actin concentration, the growth rates in equations S.1a-b will be proportional to expressions $\propto (F - c_1A - c_2B)A$ and $\propto (F - c_1A - c_2B)B$, respectively. Magnitude of kinetic rates corresponding to these terms are likely comparable to the kinetic rates corresponding to the mechanical terms ($\approx 0.01/\text{sec}$) as the actin turnover times are tens of seconds²³.

Using the derivations and scaling of the previous paragraphs, we arrive at non-dimensional equations (we keep the same notations for the non-dimensional variables):

$$\frac{\partial A}{\partial t} = (1 + \kappa_1 V(\theta))A - A^2 - a_{12}AB + D \nabla_\theta^2 A \quad \text{S.2a}$$

$$\frac{\partial B}{\partial t} = (1 - \kappa_2 V(\theta))B - B^2 - a_{21}AB + D \nabla_\theta^2 B \quad \text{S.2b}$$

$$V(\theta) = \frac{A(\theta)^m}{A(\theta)^m + A_0(T)^m} - \frac{B(\theta)^m}{B(\theta)^m + B_0^m}, T = \frac{\text{Area}^{s+1}}{\text{Area}^s + \text{Area}_0^s} \quad \text{S.2c}$$

In Eq. S.2b, we substitute $(a_{21}-a_{12})$ for a_{21} and $(a_{12} + d_{12})$ for a_{12} (keeping the same notation).

Implementation of the moving boundary and model simulation

In the simulations, we solve the first two reaction-diffusion equations (Eq. S.2a and S.2b) using forward Euler integration in time and central finite difference in space on the periodic cell boundary. Using the calculated values for A and B at each time step, we then calculate $V(\theta)$ using Eq. S.2c. The boundary movement is solved using a 1D boundary-fitted approach²⁴. Briefly, the boundary is first discretized into equally-spaced nodes at time 0. The nodes are displaced at each simulation step along the surface normal by a distance $V(\theta)dt$. A numerical coordinate transformation is performed after each step to bring the nodes to be uniformly spaced again. The main advantage of this method is that the integration of the reaction-diffusion equations is considerably simplified because the equations are solved on a uniformly spaced grid with only the spacing

between grid points changing. A crucial condition in this numerical solution is mass conservation of the combined branched and bundled actin networks. This is accomplished by the following algorithms.

Our model of the moving cell is based on the Graded Radial Extension model (GRE), first applied to the study of cell shape and dynamics in ²⁵. GRE amounts to solving the equation

$$\frac{d\vec{r}(s_0, t)}{dt} = u(s_0, t)\vec{n}(s_0, t), \quad (\text{S.3})$$

where $\vec{r}(s_0, t)$ is the position vector of the curve modeling the cellular boundary, $\vec{n}(s_0, t)$ is the unit normal of the curve, t is the time, s_0 can be pictured as an index denoting the boundary element pointed to by $\vec{r}(s_0, t)$, and $u(s_0, t)$ is the local retraction/protrusion rate depending on the sign (-/+) of u . The boundary condition is periodic, so that $\vec{r}(s_0, t) = \vec{r}(s_0 + l_0, t)$, for some $l_0 > 0$.

The time derivative on the left hand side of Eq. S.3 is an absolute derivative instead of a partial derivative. This distinction is important because the definition of the index s_0 may depend on t . In the typical formulation of GRE (based on the ball-spring model), s_0 is generally independent of t so that $\frac{d}{dt} = \frac{\partial}{\partial t}$. When s_0 depends on t

we have to use the material time derivative

$$\frac{d}{dt} = \frac{\partial}{\partial t} + \frac{\partial s_0}{\partial t} \frac{\partial}{\partial s_0}. \quad (\text{S.4})$$

If u is independent of s_0 but depends on \vec{n} , this equation is called Wulff equation in the field of crystal growth and has been shown to be connected to phenomenons with singularities such as traffic jam and shock-waves. If in addition, u depends on \vec{r} , then it has application to smectics on curved substrates where defects are known to form spontaneously because of competition between the substratum curvature and the splay energy cost for laying smectic onto a curved surface.

Aside from the possibility of singularity, the GRE equation contains another difficulty, namely how to choose s_0 . One way to see the problem is to ask what happens if it is chosen arbitrarily. The answer is best determined using an example. Suppose we have chosen s_0 to be indexed based on the arc-length at time $t = 0$. We note that s_0 will unlikely be the the arc-length at a later time. The consequence of this is that the calculation of the surface normal $\vec{n}(s_0, t)$ at a later time would involve higher spatial derivatives of \vec{r} as in the equation

$$-\frac{\vec{r}(s_0, t)}{R(s_0, t)} = \left(\frac{\vec{r}'}{|\vec{r}'|} \right)' = \frac{\vec{r}''}{|\vec{r}'|} - \frac{1}{2} \frac{\vec{r}' \cdot (\vec{r}')'}{|\vec{r}'|^3} \quad (\text{S.5})$$

where $R(s_0, t)$ is the radius of curvature. We use the apostrophe ' to denote the partial derivative with respect to s_0 . The result of this particular choice transforms the first order GRE equation (S.3) into an higher order nonlinear PDE. In general, different choices of s_0 will lead to different forms of Eq. S.3. Furthermore, because both the myosin and actin fields are defined on the boundary curve and are coupled dynamically to it, the equations describing the dynamics of these fields will also be dependent on the choice of s_0 . For example the Laplacian operator in S.1a and S.1b would have to take into account the changing s_0 .

A way to choose s_0 is to ensure that \bar{n} can be found trivially. The typical solution is to use the arc-length parametrization (i.e. $|\bar{r}'(s_0, t)| = 1$) for all t . With this particular parameterization, we have (i) a convenient equation for the outward normal of a curve in 2D, $\bar{n} = \hat{z} \times \bar{r}'$ where \hat{z} is the unit normal pointing outward from the plane of the cell, and (ii) because s_0 corresponds to real physical spacings, the partial derivative $\frac{\partial}{\partial s_0}$

has now the usual meaning of a spatial derivative along the curve, and we can take $\frac{\partial^2}{\partial s_0^2}$ as the Laplacian operator, as if the density fields evolved on a flat 1D space instead of a on a curve.

The problem of course is that s_0 at different times will differ. And we need to determine $\frac{\partial s_0}{\partial t}$ in order to determine the material time derivative in Eq. S.4. To distinguish the two parametrizations (static versus dynamic) we shall denote the later with variable s instead of s_0 . Accordingly, $s = s(t)$ is dependent on time and s_0 is independent of time and refers to the indexing at time $t = 0$. To convert between the two formulations, we need to determine $s(t)$ given that $s(0) = s_0$.

Consider two proximal points at time $t = 0$ with 'labels' s_0 and $s_0 + ds_0$. These points will be evolved to points with new 'labels' s and $s + ds$ at $t = dt$. The GRE dynamic after integrating a single step means

$$\bar{r}(s_0, 0) \rightarrow \bar{r}(s_0, 0) + u(s_0) \hat{z} \times \partial_{s_0} \bar{r}(s_0, 0) dt = \bar{r}(s, dt) \quad (\text{S.6a})$$

$$\bar{r}(s_0 + ds_0, 0) \rightarrow \bar{r}(s_0 + ds_0, 0) + u(s_0 + ds_0) \hat{z} \times \partial_{s_0} \bar{r}(s_0 + ds_0, 0) dt = \bar{r}(s + ds, dt) \quad (\text{S.6b})$$

We subtract equation (S.6b) from (S.6a) and find the 'length' on both sides by squaring

$$ds^2 = ds_0^2 + ds_0 dt \left(\left| \partial_{s_0} u(s_0) \hat{z} \times \partial_{s_0} \bar{r}(s_0, 0) \right|^2 ds_0 dt + ds_0 2u(s_0) \bar{r}'(s_0, 0) \cdot \hat{z} \times \partial_{s_0}^2 \bar{r}(s_0, 0) \right). \quad (\text{S.7})$$

Up to first order in dt , we obtain

$$ds^2 = ds_0^2 - 2ds_0^2 dt \left(u(s_0) (\hat{z} \times \hat{r}'(s_0, t)) \cdot \partial_{s_0}^2 \hat{r}(s_0, t) \right) = ds_0^2 + \frac{2u(s_0)}{R(s_0)} ds_0^2 dt \quad (\text{S.8})$$

or

$$\frac{\frac{(ds)^2}{dt} - 1}{(ds_0)^2} = \frac{2u(s_0)}{R(s_0)} \quad (\text{S.9})$$

Equation (S.9) describes how a cell boundary segment of length ds_0 at time $t = 0$ changes under the GRE dynamics after a duration of time period of dt . Note that the segment length remains the same in time if either $u = 0$ around the segment (which means the boundary is neither expanding nor shrinking) or $R \rightarrow \infty$ (which implies that a straight segment maintains a constant length even when in motion; only curved segments undergo expansion or contraction when the boundary deforms).

We define $\frac{dl}{ds_0} = \frac{ds - ds_0}{ds_0}$ and note that $\frac{(ds)^2}{(ds_0)^2} - 1 = \left(2 + \frac{dl}{ds_0} \right) \frac{dl}{ds_0}$. If we take the limit as dl approaches zero in equation (S.9) we obtain:

$$\frac{dl}{dt} = \frac{ds - ds_0}{dt} = ds_0 \frac{u(s_0)}{R(s_0, 0)}. \quad (\text{S.10})$$

By integration over the cell curve

$$\int_0^{s_0} ds = \int_0^{s_0} ds_0 + dt \int_0^{s_0} ds_{0'} \frac{u(s_{0'})}{R(s_{0'}, 0)}, \quad (\text{S.11})$$

which turns into

$$s(s_0, dt) = s_0 + dt \int_0^{s_0} ds_{0'} \frac{u(s_{0'})}{R(s_{0'}, 0)}, \quad (\text{S.12})$$

we obtain the final result

$$\frac{\partial s}{\partial t} = \int_0^s \frac{u(s')}{R(s')} ds'. \quad (\text{S.13})$$

We have dropped the subscript zero so that the indexing on the right hand side simply refers to the current indexing scheme since time $t = 0$ can be chosen arbitrarily.

In essence, the above steps represent a coordinate transformation of the problem into a system that makes the equations easier to solve numerically – from the static, fixed index s_0 to the dynamic coordinate system defined

using the arc-length parameter at each time frame $s(t)$. This transformation is similar to the method of fitted boundary in the free boundary problem. A convenient by-product of using this transformation is that the dynamical equations of the densities take on a particularly simple form.

Let φ be a density field that undergoes reaction and diffusion on the boundary curve. Since the transformed index (coordinate) $s(t)$ refers to the actual physical spacing (arc-length), the dynamic equation for φ at any fixed time can be written in a 1D space

$$\frac{\partial \varphi}{\partial t} = D_{\varphi} \frac{\partial^2 \varphi}{\partial s^2} - \frac{\partial}{\partial s} \left(\frac{\partial s}{\partial t} \varphi \right) + \beta(s(t), t) \quad (\text{S.14})$$

where $\beta(s(t), t)$ denotes the reaction part. The first term on the right represents diffusion; the second term accounts for the fact that the density field is associated with the material point associated with index s and therefore evolves with it. We may expand the second term into

$$-\frac{\partial}{\partial s} \left(\frac{\partial s}{\partial t} \varphi \right) = -\frac{\partial s}{\partial t} \frac{\partial \varphi}{\partial s} - \frac{\partial}{\partial s} \left(\frac{\partial s}{\partial t} \right) \varphi = -\frac{\partial \varphi}{\partial s} \int_0^s \frac{u(s')}{R(s')} ds' - \frac{u(s)}{R(s)} \varphi. \quad (\text{S.15})$$

The final term of this equation is particularly interesting. Suppose we have a circular cell and it is expanding uniformly so that $u/R > 0$, the final term says that φ will decrease at a rate proportional to φ . This reflects the fact that expanding cells increase surface by density dilution/concentration.

For the record, we summarize the GRE equation in component form below

$$\frac{\partial r_x}{\partial t} = -u \frac{\partial r_y}{\partial s} - \frac{\partial s}{\partial t} \frac{\partial r_x}{\partial s}, \quad \frac{\partial r_y}{\partial t} = u \frac{\partial r_x}{\partial s} - \frac{\partial s}{\partial t} \frac{\partial r_y}{\partial s}, \quad \frac{\partial s}{\partial t} = \int_0^s \frac{u(s')}{R(s')} ds' \quad (\text{S.16})$$

These sets of equation can be numerically solved using standard methods. We use explicit Euler method with first-order upwinding.

Predicted behavior

We systematically varied the two parameters a_{12} and a_{21} characterizing bundling and centripetal flow rates, respectively, to obtain the motility phase diagram (Fig. 5a). The phase diagram shows the different combinations of the two parameters that would lead to cell polarization and movement. In general, when both bundling rate and centripetal flow rate are of the same order of magnitude (along the diagonal in the phase diagram), the cell is more likely to polarize and move. In the motile regimes, the bundled actin and branched actin spatially segregate (Fig. 5a and Supplementary Fig. 4a) to the rear and front of the cell respectively. This spatial segregation is maintained by the positive feedback between cell movement and actin dynamics. The only exception to the general rule is when both a_{12} and a_{21} are very small compared to 1 (Supplementary Fig. 4a, Cell I); In this part of the phase diagram, the cell remains un-polarized because neither bundled actin nor branched

actin is dense enough to dominate the system. In fact, they coexist and maintain a stable balance, keeping the cell in the un-polarized state.

If the bundling rate becomes much greater than the centripetal flow rate, then the bundled actin-myosin ring dominates around the whole periphery and the cell remains round and non-motile (Fig. 5a, Cell A). If the bundling rate becomes much less than the centripetal flow rate, then the branched actin network dominates around the whole periphery, but the actin growth is stalled by the membrane tension everywhere, and the cell remains round and non-motile (Fig. 5a, Cell D). Because the bundling rate is expected to increase with the strength of myosin, the model predicts that at high myosin strength (control cell), there is a high density of bundled actin and low density of branched actin around the periphery, and these densities are constant along the boundary, and the cell is not polarized. On the other hand, at very low myosin strength, there is a high density of branched actin but very low density of bundled actin around the periphery, and again these densities are constant along the boundary, and the cell is not polarized.

When cells do become polarized, the steady state shape depends on the relative magnitude of the bundling rate (a_{12}) and centripetal flow rate (a_{21}). For example, decreasing the bundling rate and keeping centripetal flow rate constant decreases the front-rear distance (Supplementary Fig. 4c). In short, the cell shape can transition smoothly from elongated fibroblast-like shapes to crescent-shaped shapes. This result is consistent with the experiment using myosin inhibitors: As discussed in the main text, the cell is stationary at control levels of myosin activity; upon treatment with 20 μM blebbistatin, the cell polarizes and the cell shape is elongated from front to rear (compare Fig. 5b [20 μM] and Supplementary Fig. 4c). At higher blebbistatin concentrations (60 μM), the stable cell shape is shorter from the front to the rear (Fig. 4B [60 μM] and Supplementary Fig. 4c).

Dependence on initial conditions

The ability of a cell to polarize by competition of branched and bundled actin species depends on the initial conditions. In our simulations, we started each run with a high bundled actin density around the cell periphery. After a short equilibration time (10τ), we significantly decreased the density of the bundled actin population over a particular cell boundary segment. The smaller the width of the perturbing segment the narrower was the region in the phase diagram corresponding to polarizing cells (Supplementary Fig. 4b). For example, the far left panel of Supplementary Fig. 4b corresponds to a case where only a small perturbation was applied. The phase diagram shows that although the cell polarizes for some combination of parameters, for the majority of the parameter space the perturbation simply relaxes to the uniform symmetric non-motile steady state. However, with increasing perturbations (the middle-panel and the right-panel), more and more area in the phase diagram

covers the motile regime. The simulation shows that increasing the perturbation further beyond that in the right panel does not change the motility phase diagram further, indicating that the last phase diagram, which corresponds to the phase diagram in Fig. 5a, maps out all possible combinations of parameters a_{12} and a_{21} that can induce motility.

Indeed, we found that even for parameter choices in the region of predicted self-polarization, the process is initiated only by a large-enough asymmetric perturbation (Supplementary Fig 4b). If either the width of a sector at the cell edge along which the density of bundled actin decreases transiently, or the magnitude of that decrease or both are too small, the fluctuations in the density ratio between branched and bundled actin relax back to the symmetric state. Note that we also repeated these simulations with initial distributions of two network densities with added spatial noise, so that the branched network density is not equal to zero, but rather is a small positive random function of the spatial coordinate, while the bundle network density is like that shown in Supplementary Fig 4b with an added small positive random function of the spatial coordinate. The results for the parameter choices in the region of predicted self-polarization are similar to the case shown in Supplementary Fig 4b. Thus, it is the width and the depth of the inhibition of the actomyosin bundling that is crucial for the cell polarization. Indeed, our experiments on micro-point ablation of circumferential actomyosin bundles with a laser beam produced a local transient increase in membrane protrusivity by apparently shifting the balance toward F-actin branching (Supplementary Video 4). However, such cells did not polarize and remained stationary as this localized perturbation was too small to promote cell scale symmetry breaking and motility initiation.

Remarkably, the model never predicted complicated ‘shape-shifters’ and cells that have many local protrusions and retractions after the symmetry is broken. We varied initial conditions specifically perturbing the symmetric cells by high spatial harmonics and complex shapes in order to test this possibility. After perturbation of the symmetric state by a) three equidistant peaks/depressions in the branched network distribution, b) three equidistant peaks/depressions in the bundled network distribution, or c) three equidistant expansion/retraction deformations in the cell shape, the cell shape and branched/bundled network densities return to the symmetric state. Similarly, perturbations by two and four equidistant peaks in both network densities and/or cell shape did not evolve into the asymmetric shape-shifting cells. The relative simplicity of the evolved motile shape can be explained with two reasons: 1) even for the model on a stationary cell, the first harmonic ($\cos(\theta)$, where θ is the polar angular coordinate around the cell boundary) is less stable than any higher harmonics when the perturbation of the symmetric state is small; 2) In the motile cell, when the perturbation of the symmetric state is large, the boundary consists of two parts – protruding and retracting. On the former, the branched network is upregulated, while on the latter, the bundled network grows faster. Thus, the motile cell corresponds to the first spatial harmonic. The higher harmonics correspond to a number of narrow, finger-like protrusions interspersed

among retractions. These modes of perturbation cannot grow far from the symmetric state: indeed, retractions in this can only proceed to the center of the cell, while protrusions become narrower as they grow due to the area conservation of the cell, and eventually protrusions cease altogether. These analyses also highlight the requirement for cell movement for perturbations to propagate into persistent polar organization of the networks. Without the ability of the cell boundary to move the competition of the branched and bundled networks is never biased and the homogeneous, symmetric state is restored.

Stochastic effects

Our experiments investigated cell polarization upon spontaneous symmetry breaking. These events are driven by constitutive fluctuations in the actin and myosin densities and do not depend on external perturbations. To recapitulate this scenario in the model, we introduced stochastic actin dynamics by adding a random term to the evolution equations for A and B, in the form of $\mu(\theta,t)X$, where $X = A$ or B respectively, and $\mu(\theta,t)$ is a random function constructed using the formula

$$\mu(\theta,t) = \delta(t)^{1/2} \sum_{k=-n}^{k=n} c_k e^{-i\phi_k - ik\theta}$$

with $n = 16$ denoting the highest harmonic mode included, and $\phi_k = \phi_{-k}$ is a uniformly distributed random number (phase) between 0 and 2π that gets randomized at every time step, and $\delta(t)$ is the Delta-function. This method is designed so that the variance of the spatial Fourier components of μ has the form $\langle \mu(k,t)\mu(-k,t) \rangle = \delta(t)c_k^2$, similar to that of a Brownian random walk. In our simulation, $c_k^2 = 0.04$ for $k \leq n$.

Adding stochastic dynamics produced more realistic motile cell shapes and movements. For example, Supplementary Fig. 4d shows a stably moving stochastic cell with parameters very close to Cell C in Fig. 5a. Notice the crescent-shaped outline despite the added fluctuations. This result suggests that cell shape and cell polarization are robust against some level of random perturbation. At a high perturbation level, the cell shape simply fluctuates without polarization and movement because the feedback between cell front and back is broken. Finally, at myosin strengths much above default levels, the stochastic simulations predicted the collapse of the cell (Supplementary Fig. 4a, cell F). In this case, the bundling term decreases the branched actin density so much that there is no protrusion counteracting myosin contraction at all and the cell periphery shrinks.

Slow global feedback due to the flow stabilizes the polarized state

As we noted in the previous sub-section, at a high random perturbation level the cell shape simply fluctuates without polarization and movement because the feedback between cell front and back is broken. However, when we analyzed the predicted behavior at various initial conditions, we discovered that only long-lasting and

spatially extensive fluctuations of the actin distribution along the boundary lead to the polarization and motility. This is in agreement with the experiment. How could we reconcile the requirements for great fluctuations to break the symmetry and initiate motility and for attenuated randomness in the polarized state to stabilize the motile cell? We propose that the answer is in the slow long-range feedback between myosin distribution and actomyosin flow created by the cell movement.

The feedback is as follows: if the polarized cell moves with speed V , then there is a relatively constant retrograde flow of the cytoskeleton in the framework of the moving cell. Assuming that myosin molecules assemble into clusters, bind to the actin network, flow with it, then disassemble, diffuse in the cytoplasm and assemble anew²⁶, myosin in the moving cell will be swept to the cell rear. Mathematically, we adapt the model by Rubinstein *et al.*²² that posits the following equations:

$$\frac{\partial M}{\partial t} = -V \frac{\partial M}{\partial x} + s_1 M_0 - s_2 M, \quad \frac{\partial M_0}{\partial t} = D \frac{\partial^2 M_0}{\partial x^2} - s_1 M_0 - s_2 M.$$

Here M is the density of the myosin associated with F-actin, M_0 is the density of myosin diffusing in the cytoplasm, x is the distance (inward) from the leading edge of the moving cell, D is the coefficient of myosin diffusion in the cytoplasm, and s_1, s_2 are the association/dissociation rates. For simplicity, let us assume that the dissociation rate is very slow and all actin-associated myosin disassembles at the very rear of the cell together with the remnants of the actin network. Moreover, let us assume that the diffusion of unbound myosin in the cytoplasm is very fast. In this case, $s_1 M_0 = S \approx \text{const}$, term $s_2 M$ can be omitted, and equation for actin-associated myosin effectively uncouples from the second equation (other than the constraint conserving total myosin). Then, the model reduces to equation

$$\frac{\partial M}{\partial t} = -V \frac{\partial M}{\partial x} - S.$$

This equation describing constant-rate assembly of myosin across the cell and its drift to the rear has to be complemented with the natural boundary condition of sweeping myosin backward from the protruding leading edge: $M(0) = 0$. This equation has the very simple stationary solution $M = \frac{S}{V} x$. This solution predicts a linear increase of myosin density from the front to the rear in the steadily moving cell, which is confirmed by our observations (Fig. 7d).

Let us recall now that the bundling term $a_{12}(M)$ is the increasing function of the local myosin density M . In the moving cell, therefore, at the leading edge the bundling rate will be very small because myosin is kept away from the front by effective drift, so the protrusion at the front is not hindered by the bundling effect. On the other hand, at the rear the bundling term is maximal, because the myosin accumulates due to the actin flow, and

the retraction conditions are favored by the rapid bundling. Therefore, this feedback between myosin and global flow stabilizes cell motility.

In order to understand why this feedback is slow, let us examine what happens if the cell speed varies with time. Specifically, let us assume that $V(t) = V_0 + \varepsilon V_1(t)$ where ε is a small parameter governing the variation. Then,

$$\frac{\partial M}{\partial t} = -V_0 \frac{\partial M}{\partial x} - \varepsilon V_1 \frac{\partial M}{\partial x} - S. \quad (1)$$

Let us look for a solution in the form $M = M_0 + \varepsilon M_1$. After gathering the term of the same order, we find that $M_0 = \frac{S}{V} x$ and $\frac{\partial M_1}{\partial t} = -V_0 \frac{\partial M_1}{\partial x} - S \frac{V_1}{V_0}$. The solution for this hyperbolic equation that

can be found by the method of characteristics is $M_1 = -\frac{S}{V_0} \int_0^{L/V_0} V_1(t-\tau) d\tau$. Here L is the cell length.

Effectively, the concentration of myosin at the rear depends on the integral of the cell speed over the time needed to move one cell body length. This makes intuitive sense: the myosin has to move from the front to the rear with the actin flow before the steady distribution of myosin in the moving cell can be reached. Thus, the characteristic time scale at which this pathway works is the cell length divided by its speed, $\approx 10 \mu\text{m} / (0.01 \mu\text{m}/\text{sec}) \approx 10^3 \text{ sec}$, one order of magnitude longer than the characteristic time of $\sim 100 \text{ sec}$ of the local fast feedbacks between branched and bundled actin and much slower than the almost instantaneous feedback to and from the membrane tension²⁷.

The solution

$$M(L) \approx \frac{S}{V_0} \left(L - \varepsilon \int_0^{L/V_0} V_1(t-\tau) d\tau \right) \approx \frac{SL}{V_0 \left(1 + \frac{\varepsilon}{L} \int_0^{L/V_0} V_1(t-\tau) d\tau \right)}$$

$$\frac{SL}{\frac{V_0}{L} \int_0^{L/V_0} (V_0 + \varepsilon V_1(t-\tau)) d\tau} = \frac{SL}{\frac{V_0}{L} \int_0^{L/V_0} V(t-\tau) d\tau}$$

indicates that the myosin concentration at the rear is inversely proportional to the integral over the cell speed over the previous ~ 1000 seconds. In strict terms this solution is valid in the perturbation limit, and at the cell rear, but conceptually we can investigate the influence of the global feedback between the cell movement/actin flow and myosin density by introducing the time-dependent myosin densities into terms $a_{12}(M)$ and investigating the model behavior.

Solving the full model with such time delay becomes very involved, so we investigated the simplified movement of a ‘one dimensional’ cell, in which we considered just the cell edge velocities at the front and rear and densities of the branched and bundled actin there:

$$\text{Front: } \frac{dA_f}{dt} = (1 + \kappa V_f) A_f - A_f^2 - a_{12} (M_f) A_f B_f - d_{12} A_f B_f + D(A_r - A_f) \quad \text{S.3a}$$

$$\text{Front: } \frac{\partial B_f}{\partial t} = (1 - \kappa V_f) B_f - B_f^2 - (a_{21} - a_{12} (M_f)) A_f B_f + D(B_r - B_f) \quad \text{S.3b}$$

$$\text{Rear: } \frac{dA_r}{dt} = (1 + \kappa V_r) A_r - A_r^2 - a_{12} (M_r) A_r B_r - d_{12} A_r B_r + D(A_f - A_r) \quad \text{S.3c}$$

$$\text{Rear: } \frac{\partial B_r}{\partial t} = (1 - \kappa V_r) B_r - B_r^2 - (a_{21} - a_{12} (M_r)) A_r B_r + D(B_f - B_r) \quad \text{S.3d}$$

$$v_f = \alpha (A_f - B_f), v_r = \alpha (A_r - B_r), V_f = v_f - \psi(t) v_r + \xi(t), V_r = v_r - \psi(t) v_f + \xi(t) \quad \text{S.3e}$$

$$M_f = M_0 - \beta \int_0^{T_0} [V_f(t - \tau) + V_r(t - \tau)] d\tau \quad \text{S.3f}$$

For brevity, we do not further discuss the non-dimensional parameters α, β, T_0 . Variable $\xi(t)$ is a normally distributed random variable representing random fluctuations of the rear and front velocities. We also simplified the actin density dependencies of the velocities preserving though their positive feedback with branched and negative feedback with bundled actin. Finally, we weakened the membrane tension mediated coupling between the front and rear using the uniformly distributed (between zero and 1) random variable $\psi(t)$. This means that protrusion at one edge slows down protrusion or accelerates retraction at the other edge but with random strength.

We simulated the model S3.a-f with and without the slow long-range flow-myosin feedback. The characteristic result without this feedback is shown in Supplementary Fig. 4e (top): in the beginning, the cell polarizes and at one cell edge the branched network is dense and the bundled actin is weak, while at the other edge the branched actin is almost extinct but the bundles are dense. However, with time, the fluctuations depolarize the cell. The characteristic result with the long-range feedback is shown in Supplementary Fig. 4e (bottom): in the beginning, the cell polarizes and then stays polarized because the movement keeps myosin density polarized, dampening the fluctuation effect. It can be easily shown that this feedback stabilizes against the noise in the actin densities, as well as against the velocity fluctuations.

Finally, note that at the very rear of the cell the remnants of the actin network have to disassemble to allow the cell rear to advance. In part, the membrane tension can crush the actin network at the rear²⁸, but also it is very likely that myosin accumulated at the rear participates in the actin disassembly, as was shown by Wilson *et al.*²³. Thus, actin-disassembling function of myosin is likely to be a part of the global slow feedback stabilizing the cell movement. Adding such function to Eq. S1a modifies the equation as follows:

$$\frac{\partial A}{\partial t} = \left(r_1 + kV(\theta) \right) A - q_{\Gamma} A^2 - q_{12} \left(\frac{M}{2} \right) \frac{AB}{43} - d \left(\frac{M}{2} \right) \frac{AB}{43} + D_{142} \frac{\partial^2 A}{\partial x^2}$$

rate of change of branched actin growth of branched actin; enhanced with local protrusion and inhibited with local retraction growth is limited at high density by lack of molecular resources bundling and competition for G-actin term myosin-driven disassembly term lateral flow

Specifically, term $(d(M)B)A$ is responsible for disappearance of the branched filaments with the rate $d(M)B$ that is assumed to be proportional to the bundled filament density because to exert action, myosin molecules have to crosslink the bundled and branched filaments, and to be an increasing function of myosin strength. Mathematically, however, this term can be combined with the bundling term:

$$\frac{\partial A}{\partial t} = \left(r_1 + kV(\theta) \right) A - q_{\Gamma} A^2 - q_{12} \left(\frac{M}{2} \right) \frac{AB}{43} + D_{142} \frac{\partial^2 A}{\partial x^2}$$

rate of change of branched actin growth of branched actin; enhanced with local protrusion and inhibited with local retraction growth is limited at high density by lack of molecular resources bundling, competition for g-actin and myosin-driven disassembly term lateral flow

and qualitatively the model conclusions remain unchanged.

Supplementary References

1. Turing, A. The chemical basis of morphogenesis. *Phil. Trans. R. Soc. Lond. B* **237**, 37-72 (1952).
2. Edelstein-Keshet, L. *Mathematical Models in Biology* (SIAM, Philadelphia, PA, 2005).
3. Lacayo, C. I. *et al.* Emergence of large-scale cell morphology and movement from local actin filament growth dynamics. *PLoS Biology* **5**, e233 (2007).
4. Zemel, A. & Mogilner, A. Motor-induced sliding of microtubule and actin bundles. *Phys. Chem. Chem. Phys.* **11**, 4821-4833 (2009).
5. Burke, T. A. *et al.* Homeostatic actin cytoskeleton networks are regulated by assembly factor competition for monomers. *Curr. Biol.* **24**, 579-585 (2014).
6. Suarez, C. *et al.* Profilin regulates F-actin network homeostasis by favoring formin over Arp2/3 complex. *Dev. Cell* **32**, 43-53 (2015).
7. Rotty, J. D. *et al.* Profilin-1 serves as a gatekeeper for actin assembly by Arp2/3-dependent and -independent pathways. *Dev. Cell* **32**, 54-67 (2015).
8. Koestler S. A. *et al.*, Arp2/3 complex is essential for actin network treadmilling as well as for targeting of capping protein and cofilin. *Mol. Biol. Cell* **24**, 2861-2875 (2012).
9. Henson, J. H. *et al.* Arp2/3 complex inhibition radically alters lamellipodial actin architecture, suspended cell shape, and the cell spreading process. *Mol. Biol. Cell.* **26**, 887-900 (2015).
10. Sambeth, R. & Baumgaertner, A. Autocatalytic polymerization generates persistent random walk of crawling cells. *Phys. Rev. Lett.* **86**, 5196-5199 (2001).
11. Carlsson, A. E. Dendritic actin filament nucleation causes traveling waves and patches. *Phys. Rev. Lett.* **104**, 228102 (2010).
12. Fife, P. C. & Peletier, L. A. Clines induced by variable selection and migration. *Proc. R. Soc. Lond. B* **214**, 99-123 (1981).
13. Meinhardt, H. Turing's theory of morphogenesis of 1952 and the subsequent discovery of the crucial role of local self-enhancement and long-range inhibition. *Interface Focus* **2**, 407-416 (2012).
14. Houk, A. R. *et al.* Membrane tension maintains cell polarity by confining signals to the leading edge during neutrophil migration. *Cell* **148**, 175-188 (2012).

15. Danuser, G., Allard, J. & Mogilner, A. Mathematical modeling of eukaryotic cell migration: insights beyond experiments. *Annu. Rev. Cell Dev. Biol.* **29**, 501-528 (2013).
16. McGrath, J. L., Tardy, Y., Dewey, C. F. Jr., Meister, J. J. & Hartwig, J. H. Simultaneous measurements of actin filament turnover, filament fraction, and monomer diffusion in endothelial cells. *Biophys. J.* **75**, 2070-2078 (1998).
17. Pollard T. D., Blanchoin, L. & Mullins, R. D. Molecular mechanisms controlling actin filament dynamics in nonmuscle cells. *Annu. Rev. Biophys. Biomol. Struct.* **29**, 545-576 (2000).
18. Rock, R. S., Rief, M., Mehta, A. D. & Spudich, J. A. *In vitro* assays of processive myosin motors. *Methods* **22**, 373-381 (2000).
19. Sase, I., Miyata, H., Ishiwata, S. & Kinosita, K. Jr. Axial rotation of sliding actin filaments revealed by single-fluorophore imaging. *Proc. Natl Acad. Sci. USA* **94**, 5646-5650 (1997).
20. Prass, M., Jacobson, K., Mogilner, A. & Radmacher, M. Direct measurement of the lamellipodial protrusive force in a migrating cell. *J. Cell Biol.* **174**, 767-772 (2006).
21. Craig, E.M., Van Goor, D., Forscher, P. & Mogilner, A. Membrane tension, myosin force, and actin turnover maintain actin treadmill in the nerve growth cone. *Biophys. J.* **102**, 1503-1513 (2012).
22. Lieber, A. D., Yehudai-Resheff, S., Barnhart, E. L., Theriot, J. A. & Keren, K. Membrane tension in rapidly moving cells is determined by cytoskeletal forces. *Curr. Biol.* **23**, 1409-1417 (2013).
23. Wilson, C. A. *et al.* Myosin II contributes to cell-scale actin network treadmilling through network disassembly. *Nature* **465**, 373-377 (2010).
24. Shyy, W. *et al.* Computational Fluid Dynamics with Moving Boundaries, Dover, Philadelphia (1996).
25. Lee, J., Ishihara, A., Theriot, J. A. & Jacobson, K. Principles of locomotion for simple-shaped cells. *Nature* **362**, 167-171 (1993).
26. Rubinstein, B., Fournier, M. F., Jacobson, K., Verkhovsky, A. B. & Mogilner, A. Actin-myosin viscoelastic flow in the keratocyte lamellipod. *Biophys. J.* **97**, 1853-1863 (2009).
27. Kozlov, M. M. & Mogilner, A. Model of polarization and bistability of cell fragments. *Biophys. J.* **93**, 3811-3819 (2007).
28. Ofer, N., Mogilner, A. & Keren, K. Actin disassembly clock determines shape and speed of lamellipodial fragments. *Proc. Natl. Acad. Sci. USA* **108**, 20394-20399 (2011).